

Quantitative phase imaging based on Fourier ptychographic microscopy: advances, applications, and perspectives

Chuanjian Zheng,^{a,b} Tianyu Wang,^c Zhan Li,^{a,b} Ruiqing Sun,^d Delong Yang,^{a,b} Sen Wang,^c Binjie Ouyang,^c Fei Liu,^c Meng Xiang,^{c,*} Qun Hao,^{a,b,e,*} and Shaohui Zhang^{a,b,*}

^aSchool of Optics and Photonics, Beijing Institute of Technology, Beijing, China

^bNational Key Laboratory on Near-Surface Detection, Beijing, China

^cSchool of Optoelectronic Engineering, Xidian University, Xi'an, China

^dSchool of Computer Science and Technology, Beijing Institute of Technology, Beijing, China

^eChangchun University of Science and Technology, Changchun, China

Abstract. Quantitative phase imaging (QPI), promoted by advances in digital holography and computational imaging, is a label-free microscopy approach to investigating phase objects that are optically transparent or translucent, such as cells, tissues, or industrial microstructures. As a computational imaging technique, Fourier ptychographic microscopy (FPM) has rapidly emerged as a powerful tool to achieve wide-field and high-resolution QPI. It can recover the quantitative phase maps of optical path length delays introduced by unlabeled samples, providing an objective measure of refractive index distribution or surface topography of samples. Over the past 12 years, ongoing advances in FPM hardware and software have led to numerous applications in biomedicine and industrial fields. Here, we review the field of QPI based on FPM (FPM-QPI), starting with the underlying principles, followed by a summary of representative advances in both algorithms and imaging models, and ending with the breadth of applications. Finally, we conclude with the emerging challenges and opportunities for the deployment of FPM-QPI as well as the application trends that can expand the scope and utility even further.

Keywords: Fourier ptychographic microscopy; quantitative phase imaging; phase retrieval; intensity diffraction tomography; deep learning.

Received Apr. 8, 2025; revised manuscript received May 20, 2025; accepted May 29, 2025; published online Jun. 27, 2025.

© The Authors. Published by Hangzhou Institute of Technology of Xidian University and Chinese Laser Press under a Creative Commons Attribution 4.0 International License. Distribution or reproduction of this work in whole or in part requires full attribution of the original publication, including its DOI.

[DOI: [10.3788/AI.2025.20001](https://doi.org/10.3788/AI.2025.20001)]

1. Introduction

Since its invention in the 1600s, the optical microscope has experienced ongoing development and has become a commonly used instrument to render small objects visible in biomedicine, material science, chemistry, and other areas^[1]. Currently, microscopy remains an active research field due to the rapidly increasing demands for providing higher spatial and temporal resolution, higher contrast, longer penetration depth, and more accurate quantitative capabilities. Quantitative phase imaging

(QPI)^[2,3] is emerging as a powerful label-free microscopy approach to visualizing cells and tissues with nanoscale sensitivity to morphology. Fourier ptychographic microscopy (FPM)^[4,5] is a superior computational imaging technique to achieve high space-bandwidth product (SBP) QPI, which bypasses the trade-off between the field of view (FOV) and spatial resolution. Here, we review the context of QPI based on FPM (FPM-QPI), the theoretical basis of FPM-QPI, the advances of FPM-QPI, and the representative applications in biomedicine and topography measurement. We also discuss the emerging challenges and opportunities that will shape future development.

In an optical microscope, light works as the carrier of the sample information and is projected onto human eyes or digital

*Address all correspondence to Meng Xiang, E-mail: xiangmeng@xidian.edu.cn; Qun Hao, qhao@bit.edu.cn; Shaohui Zhang, zhangshaohui@bit.edu.cn

image sensors to form intensity images. For human observation, a high-quality image must be presented with varying degrees of light intensity and colors in the visible spectrum. This requirement implies that spatial resolution and contrast are two central metrics in microscopy. In 1873, Abbe proposed the first theory of image formation of the microscope: the ultimate image is formed by the superposition of light waves propagating at different angles from the sample^[6], determining that the accessible spatial resolution is ~ 200 nm when using wave optics^[7]. This resolution criterion remained unchanged until Hell and Wichmann proposed stimulated-emission-depletion (STED) fluorescence microscopy in 1994. Therefore, the other metric of imaging, contrast, has attracted tremendous research interest during the long history of more than a century. A common issue in microscopy is the poor contrast produced when light passes through transparent samples or reflects from surfaces with high reflectivity. Various optical techniques^[8] have been developed to increase the contrast for such samples. Zernike phase contrast^[9,10] and Nomarski differential interference contrast^[11] are two widely used methods that leverage the phase shift of light caused by the varying refractive index (RI) of the sample to obtain enough image contrast. However, the image intensity of the two methods is not linearly related to the corresponding phase shift. In addition, the halo and shade-off artifacts, together with phase contrast methods, also hinder the subsequent image analysis and processing^[12,13], such as cell counting and segmentation.

Alternatively, QPI enables label-free quantification of optical path differences by measuring the phase shift distribution across the entire FOV, establishing itself as a powerful tool for both biomedical characterization and industrial inspection. In biomedical applications, the quantitative phase map correlates with fundamental cellular properties, providing non-invasive measurements of dry mass distribution^[14,15,20], cell growth^[16,17], and dynamics of intracellular transport^[18,19]. For industrial metrology, this technique has demonstrated exceptional sensitivity in microstructural height profiling and surface topography reconstruction. Among existing QPI modalities, FPM has garnered significant attention due to its unique capability to transcend inherent trade-offs in conventional microscopy.

The foremost advantage of FPM lies in its ability to overcome the coherent diffraction limit of a low numerical aperture (NA) objective, achieving high-resolution (HR) phase mapping while retaining the inherently wide FOV characteristic of a low-NA system^[4]. This breakthrough is accomplished through a computational synthesis of angle-varied illuminations rather than mechanical scanning. Furthermore, FPM exhibits three distinctive merits compared to conventional interferometric QPI: 1) Adaptive aberration correction with algorithmic processing^[50,54] enables accurate QPI under spatially and temporally varied aberration; 2) high compatibility with commercial microscope platforms enables easy implementation and concise configuration; and 3) partially coherent illumination with a light-emitting diode (LED) array enables speckle-free high-quality imaging. These attributes together enable FPM to provide robust phase quantification in diverse scenarios ranging from live-cell imaging to semiconductor wafer and glass inspection.

In this review, we first introduce the underlying principle of FPM-QPI implementation, mainly focusing on the basic forward imaging model and phase retrieval algorithm. Subsequently, we trace the advances in algorithms and imaging models developed to address the limitations of the original FPM-QPI. Finally, we highlight the application in biomedicine

and topography measurements and three key ongoing research trends that will facilitate the process of deploying the FPM-QPI method in commercial platforms in the future.

2. Underlying Principles of FPM-QPI

2.1 Non-interference quantitative phase imaging

When it comes to phase measurement or QPI, interferometry will automatically occur for many people. Since the invention of lasers in 1960, most phase measurement methods have been gradually established based on interferometry. Nowadays, interferometry has become a prominent role in optical metrology. A high-precision interferometer can produce an extremely sensitive phase measurement with the optical path accuracy up to $\lambda/100$, where λ is the wavelength of lasers. With the development of interferometry over half a century, many branches of interferometry have evolved, including interferometric microscopy^[20–22], diffraction phase microscopy^[23,24], and digital holography^[25–28]. Despite the advances of these techniques, their basic principle of operation remains essentially unchanged. To render the high-frequency-oscillated light wave ($\sim 10^{14}$ Hz^[29]) recordable for current image sensors ($< 10^8$ Hz), the object beam is superposed with a reference beam to generate intensity variation, i.e., the interference pattern. However, due to the high requirement for the coherence of the two light beams and the sensitivity to disturbance, the complex optical configurations are unavoidable, and the associated speckle noise will also limit the imaging resolution.

In recent years, low-coherence interferometric microscopy has gradually attracted researchers. They combine broadband illumination with a common-path configuration to address the speckle noise and improve the stability of mechanical vibration and air fluctuation. Many techniques have emerged and have shown their powerful performance of QPI, such as spatial light interference microscopy (SLIM)^[30], quadriwave lateral shearing interferometry (QWLSI)^[31], and white-light diffraction phase microscopy (wDPM)^[32]. However, most of them still require complicated systems that are not compatible with commercial microscopes, hindering their widespread use in clinical diagnosis and life science.

Indeed, interference is not the only way to convert the unmeasurable phase information into measurable intensity variation. Propagation of light fields and asymmetric illumination are also two common approaches to achieving the phase-to-intensity conversion. Based on the propagation approach, the transport of intensity equation (TIE)^[33–35] provides a non-interferometric way to obtain quantitative phase information by measuring the intensity variation from focused to defocused planes. Through asymmetric illumination, differential phase contrast (DPC)^[36–38] can retrieve quantitative phase information by capturing intensity images under multiple asymmetric and complementary illuminations. To recover the loss phase information from intensity measurements, whether TIE or DPC, they need to model the forward physical process of intensity image formation and seek the solution by inverting the model, i.e., solve the inverse problem. Such non-interferometric QPI techniques are called phase retrieval^[39,40]. However, due to the competition between spatial resolution and imaging FOV, the SBP^[41] of the two methods is limited to around megapixels. They can provide either a QPI image with a small FOV and fine details or an image with a wide FOV and coarse details.

To break the intrinsic trade-off of FOV and spatial resolution, FPM-QPI introduces another innovation in classical optics: synthetic aperture imaging^[42]. Synthetic aperture imaging was first designed for large radio telescopes, aiming to bypass the resolution limit of a single telescope. Since the resolution of an imaging system is proportional to the lens aperture size, the radio imaging resolution can be significantly improved by synthesizing images from several telescopes. Stitching these images together is possible because the full complex field (amplitude and phase) can be directly recorded at radio wavelengths. However, no phase information is directly measured in the visible wavelength. Instead, FPM-QPI indirectly recovers the missing phase information from intensity measurements during an iterative phase retrieval process. The elegance of FPM-QPI lies in that it achieves synthetic aperture naturally along with the phase retrieval process. As a result, FPM-QPI can use an objective with low NA to achieve QPI with high resolution and maintain the original wide FOV.

To realize accurate FPM-QPI, the key points are basically the same as those in other phase retrieval techniques: 1) model a

more accurate forward physical process of intensity image formation; 2) seek more accurate phase retrieval algorithms to solve the inverse problem. The two points have stimulated the development of multiple FPM-QPI branches over the past 12 years, as shown in Fig. 1. After introducing the underlying principles, we conclude the primary approaches that have had a significant impact on modern FPM-QPI methods or have the potential to solve current challenges: phase retrieval algorithms, intensity diffraction tomography (IDT), and artificial intelligence (AI).

2.2. Forward imaging model

FPM is inherently a phase retrieval algorithm, where the missing phase information is converted into intensity variation in recorded images. To retrieve the phase information, the first step is to model the physical model of the optical system and use the model to depict the intensity image formation mathematically. The schematic diagram of a typical FPM system configuration is shown in Fig. 2(a). The system can be built by replacing the condenser of a commercial microscope with a programmed

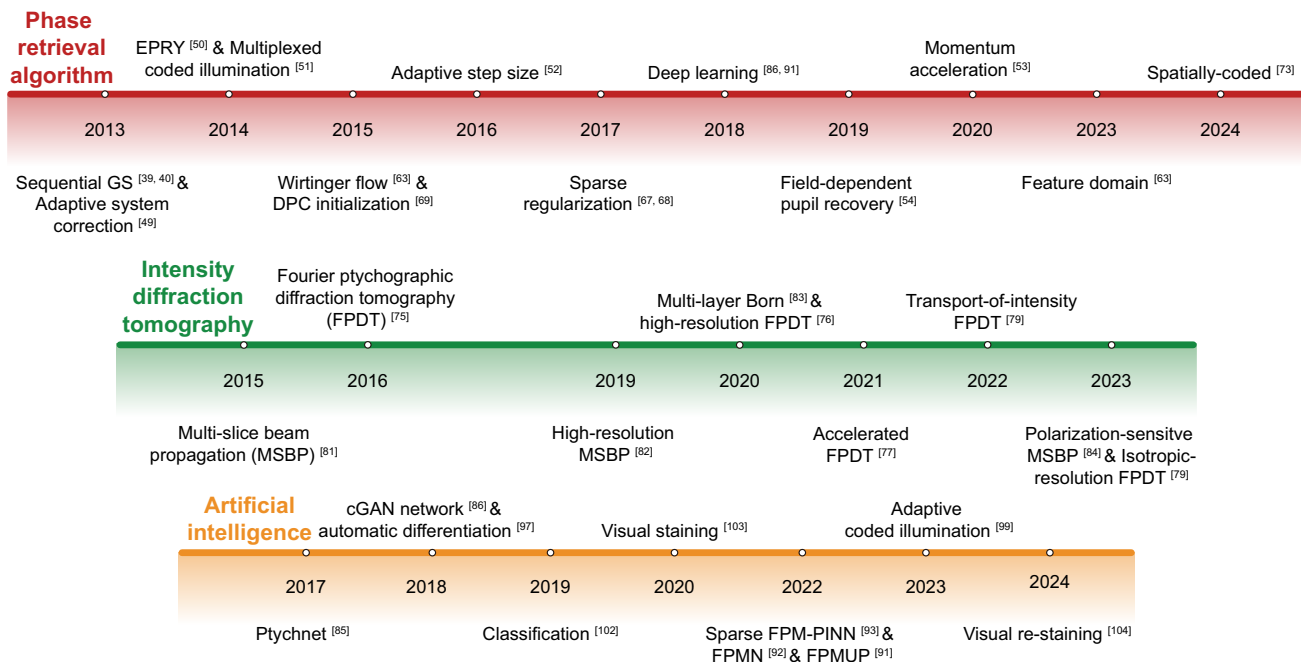


Fig. 1 FPM-QPI has evolved into three branches stimulated by advances in the forward imaging model and the phase retrieval algorithm. Schematic of the three main branches: phase retrieval algorithm, intensity diffraction tomography, and deep learning are indicated. The progress of the main events is listed in the timeline. The citations are showcased as follows: Phase retrieval algorithm: sequential Gerchberg–Saxton^[39,40], adaptive system correction^[49], embedded pupil function recovery (EPRY)^[50], multiplexed coded illumination^[51], Wirtinger flow^[63], differential phase contrast (DPC) initialization^[69], adaptive step size^[52], sparse regularization^[67,68], deep learning^[86,91], field-dependent pupil recovery^[54], momentum acceleration^[53], feature domain^[63], and spatially-coded^[73]. Intensity diffraction tomography: multi-slice beam propagation (MSBP)^[81], Fourier ptychographic diffraction tomography (FPDT)^[75], high-resolution MSBP^[82], multi-layer Born^[83], high-resolution FPDT^[76], accelerated FPDT^[77], transport-of-intensity FPDT^[80], polarization-sensitive MSBP^[84], and isotropic-resolution FPDT^[79]. Artificial intelligence: PtychNet^[85], conditional generative adversarial network (cGAN)^[86], automatic differentiation^[97], classification^[102], visual staining^[103], sparse FPM-PINN^[93], Fourier ptychography multiparameter neural network (FPMN)^[98], FPM using untrained deep neural network priors (FPMUP)^[91], adaptive coded illumination^[99], and visual restaining^[104].

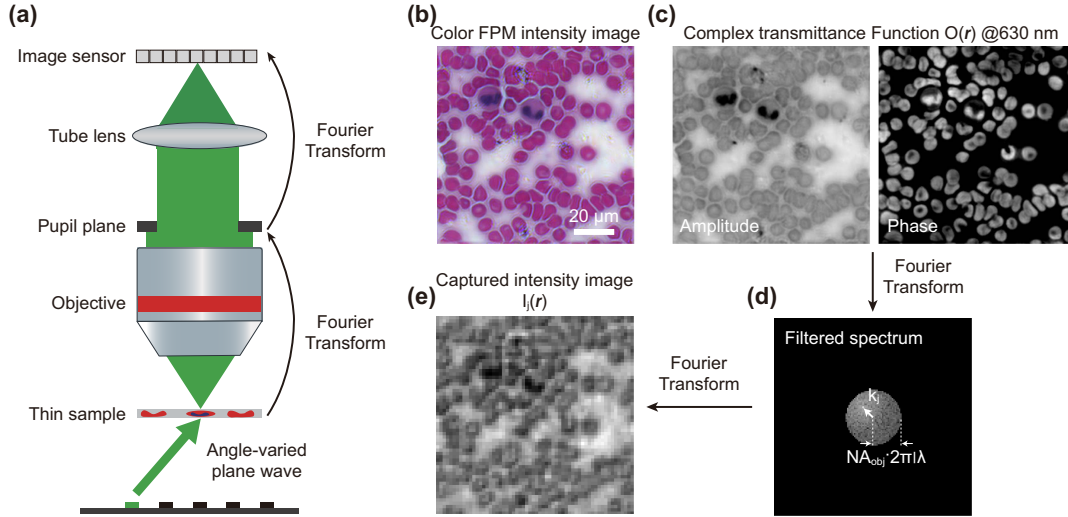


Fig. 2 Forward imaging model of FPM-QPI for thin samples. (a) Schematic diagram of system configuration. (b) Color high-resolution FPM intensity image of a thin blood smear. (c) The complex transmittance function consists of amplitude and phase at 630 nm wavelength. (d) Low-pass filtered spectrum at the pupil plane. (e) Captured intensity image on the image sensor.

LED array^[4]. The LED elements are successively lit up to illuminate the sample from different angles. At each angle, the image sensor records a low-resolution (LR) intensity image.

In original FPM, the sample is assumed to thin infinitely [e.g., the blood smear in Fig. 2(b)] and is described by a two-dimensional (2D) complex transmittance function $O(\mathbf{r}) = a(\mathbf{r}) \exp[i\varphi(\mathbf{r})]$, where a and φ are the amplitude and phase of sample, respectively, i is the unit imaginary number, and $\mathbf{r} = (x, y)$ represents the 2D spatial coordinate. Figure 2(c) illustrates the complex transmittance function at 630 nm. It is noted that the amplitude and phase are not fixed but vary with the illumination wavelength. For samples with hematoxylin and eosin (H&E) staining, the amplitude under red and blue lights is generally lower than that under blue light. For phase samples, the longer the wavelength, the smaller the phase delay.

The physical process of an intensity image formation is shown in Figs. 2(d) and 2(e). In the FPM system, the distance between the LED array and the sample is adjusted to be large enough so that the illumination wave emitted from the j th ($j = 1, 2, \dots, N$) LED can be considered as a plane wave $e^{i\mathbf{r} \cdot \mathbf{k}_j}$, where \mathbf{k}_j denotes the transverse wave vector. After the light wave passes through the sample, the objective performs the first Fourier transform on the light wave, which is equivalent to shift the sample spectrum by a distance of $|\mathbf{k}_j|$ along the wave vector direction. Due to the limited acceptance angle of the objective, the shifted spectrum $\hat{O}(\mathbf{k} - \mathbf{k}_j)$ is low-pass filtered by the pupil function $P(\mathbf{k})$ with a cutoff frequency of $\text{NA}_{\text{obj}} \cdot 2\pi/\lambda$, where $\mathbf{k} = (k_x, k_y)$ represents the 2D spatial frequency coordinate and NA_{obj} is the NA of the objective. Finally, the tube lens performs the second Fourier transform for the filtered spectrum to form one intensity image on the image sensor. The mathematical form of the forward model for the j th captured intensity image can be expressed as

$$\begin{aligned} I_j(\mathbf{r}) &= |\mathcal{F}\{\mathcal{F}\{O(\mathbf{r})e^{i\mathbf{r} \cdot \mathbf{k}_j}\} \cdot P(\mathbf{k})\}|^2 \\ &= |\mathcal{F}\{\hat{O}(\mathbf{k} - \mathbf{k}_j)\} \cdot P(\mathbf{k})|^2. \end{aligned} \quad (1)$$

According to the forward model, one LED illumination can generate one intensity image whose spectrum contains information of a shifted and low-pass filtered sample spectrum. In the following sections, we use the word “sub-spectrum” as shorthand for the shifted and low-pass filtered sample spectrum. FPM uses N LEDs to provide illumination. The sample spectrum is scanned tile by tile to form N intensity images containing information of N sub-spectra. It is noted that, when the sub-spectrum is moved outside the incoherent spectrum passband ($|\mathbf{k}_j| > \text{NA}_{\text{obj}} \cdot 2\pi/\lambda$), the captured intensity image becomes a darkfield image that enables phase retrieval with high-frequency information beyond the NA limit of the used objective. Importantly, to guarantee accurate phase retrieval, data redundancy (i.e., overlapping data between adjacent sub-spectra) is required to resolve ambiguities in the solution. Generally, the overlapping ratio should be no smaller than 40%^[4,43–45]. For a system with optical aberration, noise, or misalignment, the ratio should be higher so that the effects of these system errors can be relieved in the solution. A specific calculation equation of the overlapping ratio can be found in Ref. [45], which is helpful for choosing the appropriate LED gap and the distance between the LED array and the sample.

2.3. Phase retrieval process

After the intensity image data are collected, FPM performs an iterative phase retrieval process to obtain sample information. The phase retrieval process is to recover the complex transmittance function O from the captured intensity images I_j . This is essentially an inverse problem that solves for the solution using the forward imaging model. We will introduce the original phase retrieval algorithm of FPM in this section, and the improved algorithms are given in Sec. 3.1.

The original FPM algorithm is developed from a sequential Gerchberg–Saxton method^[39,40], which is a type of alternating projection applied for spatial ptychography^[46,47]. In contrast to ptychography, which records diffraction pattern diversity by scanning an aperture-limited illumination “probe” wavefront

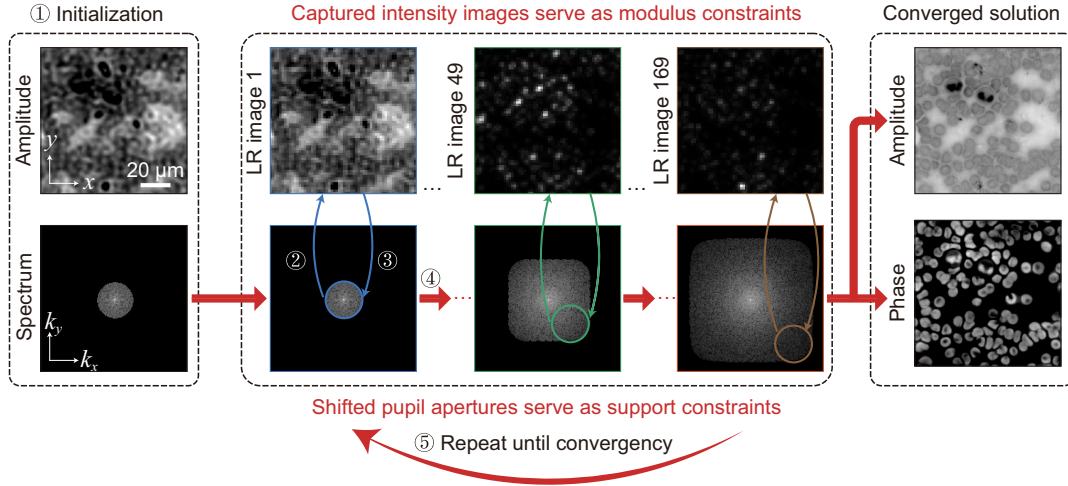


Fig. 3 Iterative phase retrieval process of FPM-QPI.

in the spatial domain, FPM introduces intensity image diversity by angle-varied illumination, where the finite pupil aperture (“probe”) of the optical system scans in the Fourier domain. The reciprocity between the two techniques allows for algorithm exchange by switching the quantities in the Fourier and spatial domains.

Figure 3 shows the iterative phase retrieval process of FPM, which is composed of five steps. The first step is to initialize the sample, where the amplitude can be set as the up-sampled LR image under normal illumination or the mean of all LR measurements, and the phase can be set as zero everywhere. Second, the current sample spectrum is shifted and constrained with the pupil function based on the forward imaging model to generate an estimated image for the j th LED as

$$\hat{O}_{j,l}^e(\mathbf{k}) = \hat{O}_l(\mathbf{k} - \mathbf{k}_j)P(\mathbf{k}), \quad O_{j,l}^e(\mathbf{r}) = \mathcal{F}\{\hat{O}_{j,l}^e(\mathbf{k})\}, \quad (2)$$

where the subscript l denotes the index of iteration, and the superscript e represents the estimated field. Third, the estimated amplitude components of the captured j th image are constrained to form an updated image and its sub-spectrum as

$$O_{j,l}^u(\mathbf{r}) = \sqrt{I_j(\mathbf{r})} \frac{O_{j,l}^e(\mathbf{r})}{|O_{j,l}^e(\mathbf{r})|}, \quad \hat{O}_{j,l}^u(\mathbf{k}) = \mathcal{F}\{O_{j,l}^u(\mathbf{r})\}, \quad (3)$$

where the superscript u refers to the field after performing the modulus constraint. Subsequently, the updated sub-spectrum is constrained with the pupil function and is shifted back to the original position to update the sample spectrum as

$$\hat{O}_{l+1}(\mathbf{k}) = \hat{O}_l(\mathbf{k}) + \frac{P^*(\mathbf{k} + \mathbf{k}_j)}{|P(\mathbf{k} + \mathbf{k}_j)|^2 + \delta_1} \times [\hat{O}_{j,l}^u(\mathbf{k} + \mathbf{k}_j) - \hat{O}_l^e(\mathbf{k} + \mathbf{k}_j)], \quad (4)$$

where δ_1 is a constant that prevents the numerical problem of dividing out the pupil function when $P(\mathbf{k} + \mathbf{k}_j) = 0$. The conjugated pupil function in the second term is used to correct the aberrated spectrum digitally, enabling an aberration-free reconstruction of sample information if the pupil function is pre-measured accurately. It is noted that it has been demonstrated that both the sample spectrum and pupil function can be

reconstructed simultaneously in the iterative process. The relevant algorithms are discussed in Sec. 3.1. In the fourth step, the second and third steps are performed for other captured images. Finally, the iterative process will be repeated several loops until the solution converges. A converged solution will cover a significantly extended spectral support in the Fourier domain. The extended spectrum has the synthetic NA (NA_{syn}) given as $NA_{\text{syn}} = NA_{\text{obj}} + NA_{\text{ill}}$, where NA_{ill} is the maximum illumination NA. The spectrum will then be transformed into the spatial domain to obtain HR amplitude and phase images.

3. Advances of FPM-QPI

3.1. Phase retrieval algorithm

The original FPM algorithm is a type of alternating projection. It can work well if the constructed forward imaging model matches the experimental system rigorously. Unfortunately, system errors, such as aberration, LED position misalignment, and noise, are generally unpredictable. In this case, the algorithm often falls into a local minimum or even fails to converge. The problem can be solved from the perspective of optimization. The core is to construct a suitable cost function that can accurately reflect the difference between the measurements and estimations. The inverse problem can be formulated as the following optimization:

$$\min_{\hat{O}(\mathbf{k})} f(\hat{O}(\mathbf{k}), P(\mathbf{k})) = \min_{\hat{O}(\mathbf{k})} \sum_{\mathbf{r}} \left| \sqrt{I_j(\mathbf{r})} - |\mathcal{F}^{-1}\{\hat{O}(\mathbf{k} - \mathbf{k}_j)P(\mathbf{k})\}| \right|^2, \quad (5)$$

where $f(\hat{O}(\mathbf{k}), P(\mathbf{k}))$ is the cost function aiming to minimize the difference between the measured and the estimated amplitudes. We note that there are also cost functions aiming to minimize the intensity difference, but the experimental robustness of which is generally not as superior as that of amplitude-based cost functions^[48]. Therefore, we consider the amplitude-based cost function in this paper.

The sample spectrum $\hat{O}(\mathbf{k})$ can be retrieved by solving the gradient of the cost function and updating $\hat{O}(\mathbf{k})$ along the direction of the gradient, which is well known as the gradient descent algorithm. One interesting thing is that alternating projection is

essentially the steepest gradient descent algorithm with a specific step size. Following a derivation analogous to that presented in Ref. [40], we can compute the direction of steepest descent for the cost function with respect to $\hat{O}(\mathbf{k} - \mathbf{k}_j)$, given by

$$-\left\{\frac{\partial f(\hat{O}(\mathbf{k}))}{\partial \hat{O}(\mathbf{k} - \mathbf{k}_j)}\right\} = 2[\hat{O}_{j,l}^u(\mathbf{k}) - \hat{O}_{j,l}^e(\mathbf{k})]P^*(\mathbf{k}). \quad (6)$$

Upon comparing the right-hand side of Eq. (4) with the direction of steepest descent given by Eq. (6), it is obvious that the update step of the original FPM algorithm can be considered as a type of gradient descent algorithm.

Inspired by advances in optimization strategies, many improved algorithms have been proposed during the past 12 years. Some representative algorithms are categorized into two groups in terms of their motivation and are summarized in Table 1.

The first group seeks to correct various system errors, including pupil aberration, LED misalignment, and noise. Three representative methods for pupil aberration correction are summarized in Table 1. The first viable method is to directly search for the Zernike coefficients that can maximize the convergence metric^[49]. However, the search process embedded within iterative recovery will be exceedingly time-consuming when the number of desired coefficients is large. The second way is to jointly recover both the sample and the pupil function during the iterative process. Similar to the sample spectrum, we can calculate the gradient of the cost function with respect to (\mathbf{k}) :

$$-\left\{\frac{\partial f(\hat{O}(\mathbf{k}), P(\mathbf{k}))}{\partial P(\mathbf{k})}\right\} = 2[\hat{O}_{j,l}^u(\mathbf{k}) - \hat{O}_{j,l}^e(\mathbf{k})]\hat{O}^*(\mathbf{k} - \mathbf{k}_j). \quad (7)$$

Following the gradient descent algorithm, we can obtain the updating formula for the pupil function:

$$P_{l+1}(\mathbf{k}) = P_l(\mathbf{k}) + \frac{\hat{O}^*(\mathbf{k} - \mathbf{k}_j)}{|\hat{O}(\mathbf{k} - \mathbf{k}_j)|^2 + \delta_2} [\hat{O}_{j,l}^u(\mathbf{k}) - \hat{O}_{j,l}^e(\mathbf{k}_j)], \quad (8)$$

where δ_2 is a constant that prevents the numerical problem of dividing out the sample spectrum when $\hat{O}(\mathbf{k} - \mathbf{k}_j) = 0$.

It is noted that, when updating the sample spectrum and the pupil function simultaneously, Eqs. (4) and (8) will not be applied directly because the signal-to-noise ratio (SNR) of high-frequency components of the measured spectrum is extremely lower than that of low-frequency components. Inspired by the extended ptychographic iterative engine (ePIE) used in spatial

ptychography, the first joint updating formula is proposed by multiplying a spatially varying step size, named the embedded pupil function recovery (EPFY)^[50]:

$$\begin{aligned} \hat{O}_{l+1}(\mathbf{k}) &= \hat{O}_l(\mathbf{k}) + \frac{|P(\mathbf{k} + \mathbf{k}_j)|^2 + \delta_1}{|P(\mathbf{k} + \mathbf{k}_j)|_{\max}^2} \frac{P^*(\mathbf{k} + \mathbf{k}_j)}{|P(\mathbf{k} + \mathbf{k}_j)|^2 + \delta_1} \\ &\quad \times [\hat{O}_{j,l}^u(\mathbf{k} + \mathbf{k}_j) - \hat{O}_{j,l}^e(\mathbf{k} + \mathbf{k}_j)] \\ &= \hat{O}_l(\mathbf{k}) + \frac{P^*(\mathbf{k} + \mathbf{k}_j)}{|P(\mathbf{k} + \mathbf{k}_j)|_{\max}^2} [\hat{O}_{j,l}^u(\mathbf{k} + \mathbf{k}_j) - \hat{O}_{j,l}^e(\mathbf{k} + \mathbf{k}_j)] \\ P_{l+1}(\mathbf{k}) &= P_l(\mathbf{k}) + \frac{|\hat{O}(\mathbf{k} - \mathbf{k}_j)|^2 + \delta_2}{|\hat{O}(\mathbf{k} - \mathbf{k}_j)|_{\max}^2} \frac{\hat{O}^*(\mathbf{k} - \mathbf{k}_j)}{|\hat{O}(\mathbf{k} - \mathbf{k}_j)|^2 + \delta_2} \\ &\quad \times [\hat{O}_{j,l}^u(\mathbf{k}) - \hat{O}_{j,l}^e(\mathbf{k}_j)] \\ &= \hat{O}_l(\mathbf{k}) + \frac{\hat{O}^*(\mathbf{k} - \mathbf{k}_j)}{|P(\mathbf{k} + \mathbf{k}_j)|_{\max}^2} [\hat{O}_{j,l}^u(\mathbf{k} + \mathbf{k}_j) - \hat{O}_{j,l}^e(\mathbf{k} + \mathbf{k}_j)]. \end{aligned} \quad (9)$$

Notice that the step size is relevant to the normalized amplitude of spectrum or the normalized amplitude of pupil function, providing a longer step size where the amplitude is higher and decreasing the step size of pixels that are higher-frequency components and may have a low SNR. The step size is a crucial factor affecting the ultimate solution. Some improved algorithms were proposed by designing different step sizes^[51–53].

Recovering aberrations with Eq. (9) is effective when the raw data are highly redundant. If the data redundancy is reduced, a prior knowledge of common optical aberrations can be introduced to the iterative recovery process. Field-dependent pupil recovery introduced the Zernike polynomials and field-dependent aberration polynomials to express pupil aberration for a full FOV^[54]. Therefore, the degrees of freedom in solution space are reduced from a 2D matrix to a small number of coefficients. The idea is also adopted in high-speed QPI where only 6 images are recorded^[55].

To correct the LED misalignment (i.e., the positional mismatch of sub-spectra), a mechanical alignment procedure is generally satisfactory if the LED arrays have a well-defined arrangement pitch^[56,57]. However, the alignment process is often time-consuming and labor-intensive. Correcting the misalignment using phase retrieval algorithms is desirable, and many algorithms have been proposed. Table 1 summarizes some of these developments. For minor misalignment, search methods with a fine initial guess are enough to refine the positions of sub-spectra^[58–60]. For large-scale misalignment, physics-based

Table 1 Representative Phase Retrieval Algorithms of FPM-QPI.

Class of Algorithm	Example	
Correct system errors	Aberration	Zernike coefficient search ^[49] , embedded pupil function recovery ^[50] , and field-dependent pupil recovery ^[54]
	LED misalignment	Simulated annealing ^[58,59] , angle self-calibration ^[60] , physics-based calibration ^[61,62] , and feature-domain ^[63,129]
	Noise	Wirtinger flow ^[64–66] , adaptive step-size ^[52] , and regularization with sample sparsity ^[67,68]
High-speed imaging	Fast capturing	Multiplexed illumination ^[51] , DPC initialization ^[67] , and low-rank recovery ^[68]
	Low redundancy	Annular illumination ^[55,69,70]

calibration strategies^[61,62] tend to outperform search methods. The effect of position misalignment can be relaxed with the feature-domain recovery algorithm, where the cost function is modified as a gradient-based cost function^[63,129].

Noise is a common problem in FPM, especially for darkfield imaging. Table 1 summarizes three kinds of algorithms to improve the robustness against noise. If we have information about the statistics of the noise, we can model the noise and use it for optimization^[64–66]. If no prior knowledge about noise statistics is known, the adaptive step size strategy for updating can be a good choice to ensure a stable convergence^[52]. In addition, one can also suppress the noise by regularizing based on the sample sparsity prior^[67,68].

The second group of phase retrieval algorithms concentrates on high-speed imaging (see Table 1). Typically, FPM requires hundreds of intensity images to provide sufficient data redundancy. This process can take tens of seconds to record, hindering real-time observation of live cells. The multiplexed phase retrieval algorithm has enabled multiple-LED illumination at one time^[51], improving both the capturing and imaging speeds. The combination of DPC initialization illumination with four semicircle patterns and darkfield multiplexing illumination strategies extremely reduced the capturing time down to ~ 0.8 s^[69]. Instead of multiplexed illumination, some methods analyzed the phase transfer features in the captured intensity images. They found that if and only if the illumination NA matches the objective NA, both the low- and high-frequency information can be converted into intensity images. Therefore, they employed only the annular illumination with the matched illumination condition to provide illumination. To ensure high-quality phase retrieval, they also adopted DPC phase initialization and achieved high-speed phase recovery with six images^[55]. Additionally, single-shot FPM is feasible by employing a multiplexed strategy along with annular illumination^[71,72].

Despite the rapid advancement in phase retrieval algorithms, the phase retrieval accuracy of FPM is sometimes unsatisfactory due to the loss of phase information in low-frequency components. This issue arises from the non-uniform phase transfer function (PTF) inherent in asymmetric-illumination microscopy^[73]. For example, when imaging a phase sample with a linear phase ramp, $\varphi(x) = x$, the captured intensity spectrum can be expressed as the product of the phase spectrum and the PTF^[80]. However, the Fourier spectrum of the phase ramp, $2\pi/(jk_x) \cdot \delta(k_x)$, corresponds to only a single zero spatial frequency component in the Fourier space. For brightfield illumination, the captured images contain only non-zero constant values. For darkfield illumination, the image intensity is zero since the zero-frequency component is excluded. As a result, these captured images offer little insight into the sample's linear phase ramp, and the recovered phase values are underestimated significantly. To address this limitation, spatially coded FPM^[73] employed a thin film attached to the sensor to encode the complex wavefront from the object, thereby providing a uniform frequency response. This approach introduces a new avenue for measurement diversity and has the potential to be adopted in various FPM systems to improve phase retrieval accuracy.

3.2. Intensity diffraction tomography

The original FPM was developed for 2D thin sample imaging, which is not applicable when the sample is thicker than the objective's depth-of-field (DOF). On the one hand, the 2D imaging

method considers the sample an infinitely thin layer. The sample information outside the DOF is not considered and, therefore, cannot be effectively recovered. On the other hand, the fact that the phase recovered with the 2D method is a product of thickness and average RI may potentially result in inaccurate characterization of samples with complex three-dimensional (3D) structures. To obtain more accurate 3D morphological information, FPM has been advanced to include 3D thick sample imaging. This method does not recover the phase delay caused by the sample; instead, it reconstructs the 3D RI distribution from captured intensity images. In this manuscript, we refer to these techniques as intensity diffraction tomography (IDT).

According to the forward imaging models, FPM-based IDT techniques can be divided into two types. The first type is Fourier ptychographic diffraction tomography (FPDT), which integrates principles of FPM and the Fourier diffraction theorem^[74] to achieve 3D QPI. As shown in Fig. 4(a), the Fourier diffraction theorem constructs the bridge linking the 2D Fourier transform of the measurement to the 3D Fourier transform of the scattering potential of the sample under the weak scattering approximation. FPDT was first demonstrated with brightfield measurements^[75]. High-angle darkfield illumination was then introduced to extend the accessible spatial frequencies^[76]. The method allowed FPDT to achieve lateral resolutions beyond the diffraction limit of the objective (e.g., 390 nm with a 0.4 NA objective). To accelerate the capturing and reconstructing process, FPDT with sparse annular LED illuminations was proposed, reducing the data requirement by more than 40 times^[77]. To address the missing cone problem resulting in a poor axial resolution several times worse than the lateral one^[78], opposite illumination FPDT combined transmissive angle-scanning and reflective wavelength scanning to obtain near-isotropic resolution (~ 274 nm)^[79]. Another key development of FPDT is to overcome the matched illumination condition: a requirement for precise alignment of illumination and objective NAs. Transport-of-intensity FPDT (TI-FPDT) leveraged the phase contrast of one additional defocus dataset to bypass the rigorous constraint^[80], significantly improving reconstruction accuracy under non-matched illumination.

The second IDT technique has evolved significantly through the integration of the multi-slice beam propagation (MSBP) model shown in Fig. 4(b), enabling HR reconstruction of volumetric RI and polarization-sensitive properties in complex scattering samples. Early advancement^[81] established a foundation by combining light field refocusing with MSBP to correct diffraction artifacts and recover 3D intensity and phase distributions, achieving lateral resolution beyond the diffraction limit of low-NA objectives. The iterative algorithm leveraged angular diversity from LED arrays to resolve thick biological samples slice by slice, demonstrating the feasibility of 3D FPM without weak scattering approximations. Subsequent work extended MSBP to address multiple scattering in optically dense samples, employing a nonlinear optimization framework to reconstruct HR 3D RI maps of multicellular organisms like *C. elegans*^[82]. Further refinements introduced the multi-layer Born (MLB) model^[83], which improved accuracy for high-angle illumination and backward scattering by decomposing the sample into slabs and iteratively applying first Born scattering. MLB retained computational efficiency while resolving axial resolution trade-offs inherent in MSBP, enabling gigavoxel-scale reconstructions of thick tissues. Recently, polarization-sensitive intensity diffraction tomography (PS-IDT)^[84] integrated vectorial

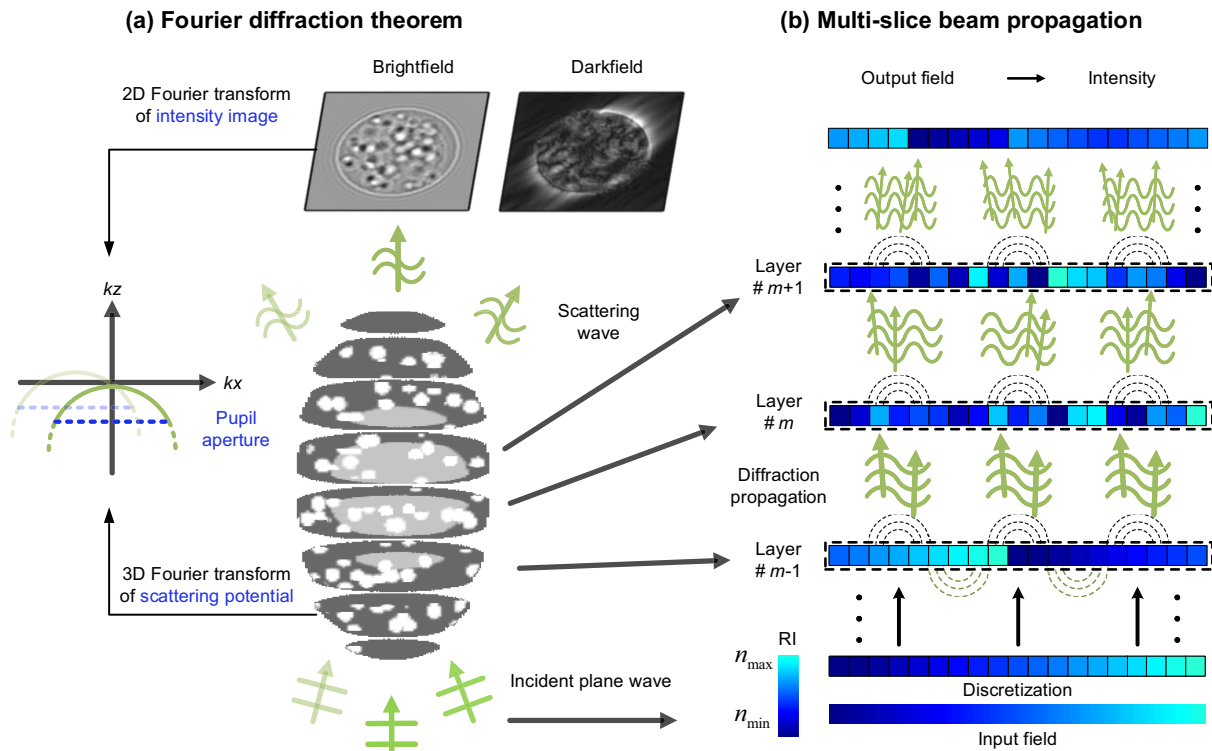


Fig. 4 Forward imaging model of 3D FPM-QPI. (a) Forward imaging model of Fourier ptychographic diffraction tomography, where the scattering potential is used to describe the 3D sample, which is a function of refractive index (RI). (b) Forward imaging model of multi-slice beam propagation, where RI is used to describe the sample that is discretized as multiple infinitely thin slices with equivalent intervals.

MSBP to recover 3D Jones matrices in anisotropic samples, addressing both isotropic and anisotropic scattering through polarization-modulated illumination. These developments underscore a trajectory toward multi-modal 3D imaging, balancing computational efficiency, physical accuracy, and versatility for diverse biological and material systems.

To better understand the advantages and disadvantages of traditional FPM and IDT, we compare them in Table 2.

3.3. Artificial intelligence

In recent years, the rapid advancement of computing power and the accumulation of high-quality data have driven explosive

developments in AI. Among these advancements, automatic differentiation tools and deep learning methods have become foundational elements, with theories continually being refined and expanded through practical applications. Their widespread adoption across numerous fields has significantly promoted research in areas of FPM-QPI.

Traditional FPM-QPI methods depend heavily on accurate physical modeling, precise system alignment, extensive prior information, and intricate analytical differential calculations. The quality of the imaging results tends to degrade significantly when actual imaging conditions deviate from theoretical modeling assumptions. In contrast, AI-based methods simplify these issues through implicit modeling approaches. Based on their

Table 2 Comparison Between Traditional FPM and IDT.

Criteria	Traditional FPM	IDT
Sample category	Thin samples (e.g., unstained slides <math><10\ \mu\text{m}</math>, adherent live cells)	Both thin and thick samples (e.g., tissues or embryos)
Recovered physical quantity	2D phase delay	3D refractive index
Raw data volume	Tens of intensity images	Hundreds of intensity images
Recovery speed	Tens of seconds (gigapixel recovery using a 4090 GPU)	Several hours (gigavoxel recovery using a 4090 GPU)
Imaging Robustness	High robustness to system errors using correction algorithms	Low robustness to system errors
Imaging throughput	0.23 gigapixels ^[4]	2.3 gigavoxels ^[62]

modeling strategies, we categorize AI-based FPM-QPI methods into three main groups: end-to-end deep learning methods, physics-based neural network methods, and physics-based automatic differentiation methods, as shown in Fig. 5.

End-to-end deep learning methods utilize deep learning models to establish direct mappings from multi-angle LR intensity measurements to HR complex field distributions, leveraging pre-prepared datasets to learn nonlinear relationships^[85,86], as shown in Fig. 5(a). Unlike traditional FPM-QPI, the approaches do not update parameters during the imaging process, enabling rapid inference and intrinsic noise suppression capabilities. PtychNet^[85] was the first work to reconstruct the image using an end-to-end deep learning neural network. Afterward, a study^[86] proposed a conditional generative adversarial network (cGAN) for dynamic live-cell FPM video reconstruction,

achieving high-fidelity phase recovery with minimal training data. The research in Ref. [87] developed a multiscale deep residual network to synthesize complex fields from intensity images, demonstrating exceptional computational efficiency and robustness. To address uncertainties in deep learning predictions, Bayesian CNN frameworks^[88] have also been proposed to quantify model and data reliability, enhancing practical applicability in time-series experiments.

Unlike end-to-end methods, physics-based neural network approaches introduce neural networks during optimization or forward modeling without requiring additional training data, as shown in Fig. 5(b). Network parameters are updated during a single imaging process to reconstruct high-quality images. Deep image priors (DIPs)^[89] first demonstrated that randomly initialized convolutional neural networks can act as handcrafted

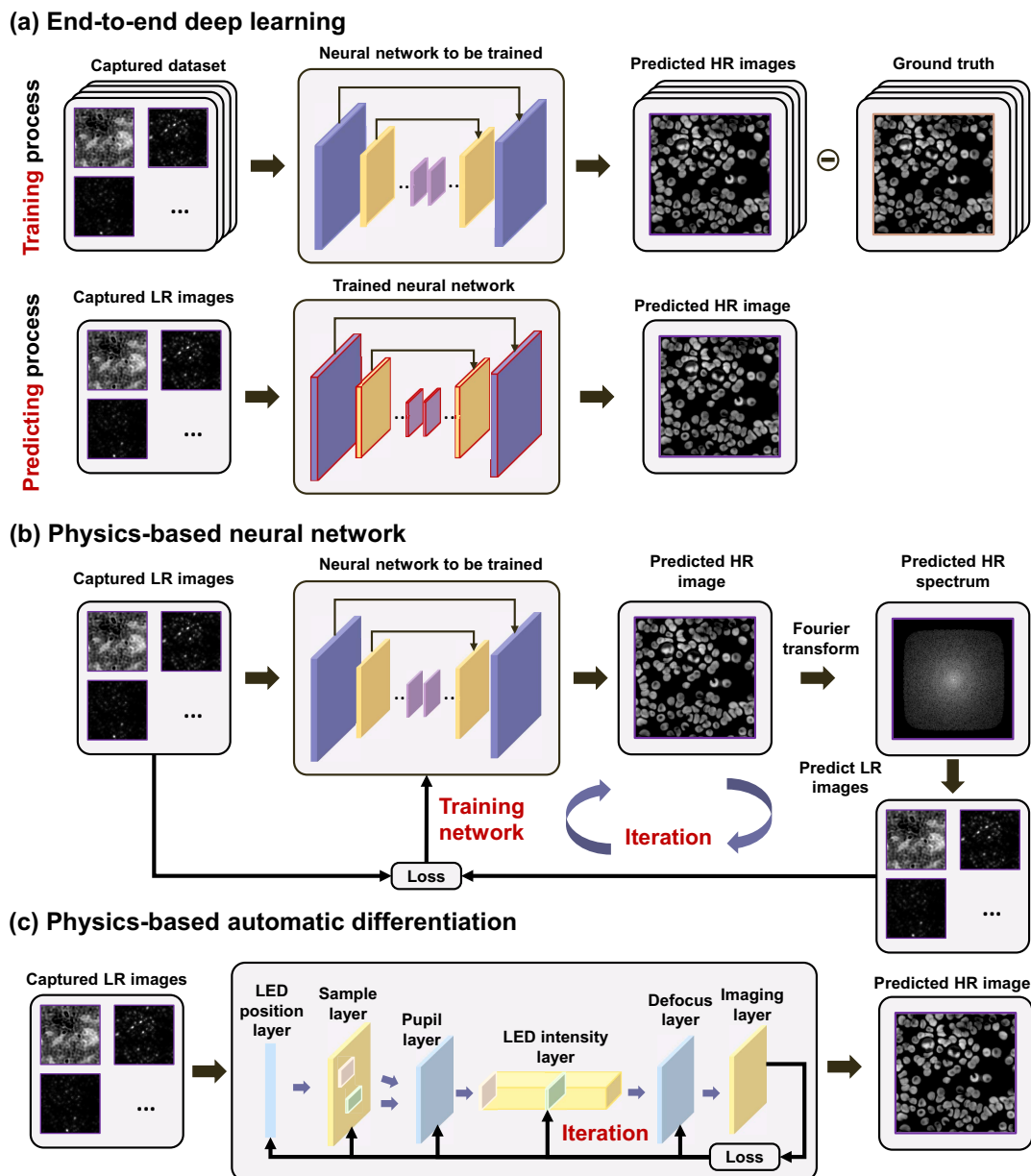


Fig. 5 Modeling strategies for three categories of AI-based FPM-QPI methods. (a) End-to-end deep learning. (b) Physics-based neural network. (c) Physics-based automatic differentiation.

priors to achieve remarkable reconstruction results. Applying DIP algorithms to subsampled FPM imaging can improve the reconstruction performance under conditions of low subsampling rates and high noise^[90]. The method was extended to separately reconstruct phase, amplitude, pupil aberrations, and illumination variations by employing four parallel untrained neural networks^[91], demonstrating significantly better image quality, particularly in phase retrieval, compared to traditional iterative algorithms. Additionally, the physics-informed neural network (PINN) approach integrates neural networks closely with physical imaging models, ensuring robust reconstruction even from limited data. By explicitly embedding physical constraints into neural network optimization, the PINN guides the optimization trajectory, thus reducing dependence on extensive experimental datasets. PhysenNet^[92], for example, combined traditional U-Net structures with imaging physics, interactively optimizing between neural networks and physical models to jointly learn network weights and biases, significantly reducing data requirements and exhibiting superior generalization. A sparse FPM-PINN method^[93] further integrated DIPs and physical models to achieve high-quality phase reconstruction under sparse sampling conditions without extra training data or labels. A hybrid framework^[94] has recently combined the data-driven priors and denoising capabilities of deep learning models with the generalization advantages of physical models, proposing a novel reconstruction approach capable of achieving high-quality image reconstruction comparable to traditional methods while reducing the required LR images by 90%.

Physics-based automatic differentiation methods utilize common automatic differentiation tools from deep learning frameworks (e.g., PyTorch, TensorFlow) to construct physical models explicitly^[95,96]. These methods incorporate physical parameters such as pupil functions, illumination variations, and LED positional errors into differentiable layers, simultaneously optimizing hardware parameters and reconstruction quality through gradient backpropagation, as shown in Fig. 5(c). An early implementation^[97] designed feedforward neural networks to simulate the FPM forward model using the point spread function or coherent transfer function, optimizing sample reconstruction by minimizing loss functions. Subsequent research FPMN^[98] introduced multiparameter networks embedding systematic errors such as pupil aberrations, illumination fluctuations, and LED positional deviations into network layers to achieve robust reconstructions. An unsupervised adaptive illumination framework^[99] incorporated a dedicated illumination pattern layer to dynamically optimize LED activation sequences, significantly reducing the number of required LR images by up to 80% and accelerating real-time data acquisition. An uncertainty-aware Fourier ptychography (UA-FP) method^[100] simultaneously addressed optical aberrations, misalignments, and low-quality data through differentiable optimization, enabling robust, high-quality imaging without the need for precise calibration. In addition, the batch-FPM scheme^[101] proposed a GPU-parallelized automatic differentiation framework based on random batching, enabling rapid and efficient image reconstruction for subsequent research and applications. Due to its unique robustness, one can perform image acquisition with uniform exposure time for both brightfield and darkfield imaging.

In addition, the recovered phase of FPM can be further processed with deep learning approaches to generate required image data in clinical diagnosis and digital pathology. A learned sensing approach^[102] co-optimized programmable LED illumination

patterns and classification networks, enhancing disease detection accuracy. The method can automatically identify malaria-infected cells with up to 5%–10% greater accuracy than standard and alternative microscope lighting designs. A virtual staining method^[103] addressed FPM's limitations in color fidelity by implementing unsupervised CycleGAN-based frameworks, effectively reducing coherent artifacts and enabling HR imaging without paired training data. Recently, a phase-to-color virtual restaining framework^[104] was proposed to restore H&E stain in faded slides. One interesting thing is that the method employed near-infrared illumination to overcome absorption variations between faded and stained samples, avoiding absorption differences between samples with various degrees of fading. The method reminds us that a straightforward visual staining technique from an unstained section to H&E or immunohistochemistry (IHC) staining may become feasible using multi-channel (visible, ultraviolet, and infrared) FPM imaging.

In summary, deep learning has redefined FPM-QPI by balancing speed, robustness, and adaptability. End-to-end methods enable fast phase retrieval with strong noise resistance, and they require little to no physical model construction. However, these methods may not always yield satisfactory results when the feature distribution of test samples significantly deviates from that of the training dataset. Physics-based neural network methods offer a promising approach to addressing data scarcity by appropriately incorporating physical principles. They exhibit strong noise resistance without necessitating highly accurate physical models. However, their reconstruction time typically range from minutes to hours. Physics-based automatic differentiation methods ensure physical consistency for any samples but require the construction of an accurate physical process. Compared to end-to-end methods, they generally require longer reconstruction time, ranging from seconds to minutes, and are more sensitive to noise. The emerging applications in clinical diagnostics and computational pathology highlight the transformative potential of these hybrid methods. We believe that the future development of these methods will focus on enhancing the real-time performance, interpretability, and generalization across various imaging systems, further consolidating FPM-QPI as a cornerstone technology in biomedical and industrial imaging^[105].

4. Applications of FPM-QPI

4.1. Label-free live-cell monitoring and analysis

Live-cell monitoring and analysis play a pivotal role in advancing biological research, enabling non-invasive observation of dynamic cellular processes and drug responses at subcellular resolution. FPM-QPI has emerged as a promising computational imaging technique in live-cell studies, addressing the inherent trade-off between spatial resolution and FOV in conventional microscopy. Early implementations of FPM utilized sequentially varying angles to illuminate samples, synthesizing gigapixel-scale phase images with both wide FOV and high resolution. However, prolonged acquisition time (minutes) limited its application to dynamic processes. A method introduced a custom high-brightness LED array and fast control circuitry to shorten the exposure time, enabling a full 173-LED scanning illumination under 7 s^[69]. The hardware improvement enabled real-time tracking of subcellular dynamics, including mitosis and lipid droplet transport in unstained cells, with automated segmentation and dry mass quantification, as shown in Fig. 6(a).

Hybrid illumination schemes combining brightfield DPC and multiplexed darkfield imaging further reduced the capture time of the system to 0.8 s while maintaining 0.8 NA resolution across a $4 \times$ FOV.

Besides the high-speed imaging requirement, long-term imaging is also desirable for live-cell monitoring. However, spatially varying aberrations and focus drifts during the process often degrade the performance of long-term imaging. An adaptive optical strategy was developed for FPM-QPI to address the limitation. By employing NA-matched annular illumination and Zernike polynomial-based aberration correction, the method achieved diffraction-limited resolution (655 nm laterally) across 1.77 mm^2 FOV for over 51 h with a frame rate of 16.66 Hz^[55], resolving organelle dynamics and multi-generational cell division, as shown in Fig. 6(b). For 3D applications, FPDT reconstructs depth-resolved RI distributions. Utilizing high-angle darkfield illumination beyond the objective NA, FPDT achieved 390 nm lateral and 899 nm axial resolution, visualizing 3D

intracellular structures across $20 \mu\text{m}$ depth *in vitro*^[76], as shown in Fig. 6(c). These representative innovations established FPM-QPI as a versatile platform for high-throughput, label-free live-cell analysis, balancing spatial-temporal resolution and volumetric imaging to capture multiscale biological phenomena.

4.2. Digital pathology and clinical diagnosis

In digital pathology, digital images of stained histology slides are acquired and used for diagnostic purposes. Compared with conventional microscopy, the phase images recovered by FPM provide a completely new dimension of information for pathologists. Mining the benefits of phase information for digital pathology and clinical diagnosis is a long-standing research topic. One early study^[106] derived tissue scattering properties via spatial variance and gradient variance of phase maps recovered from stained pathological slides to reveal microscale heterogeneity, as shown in Fig. 7(a). Visual staining based on the

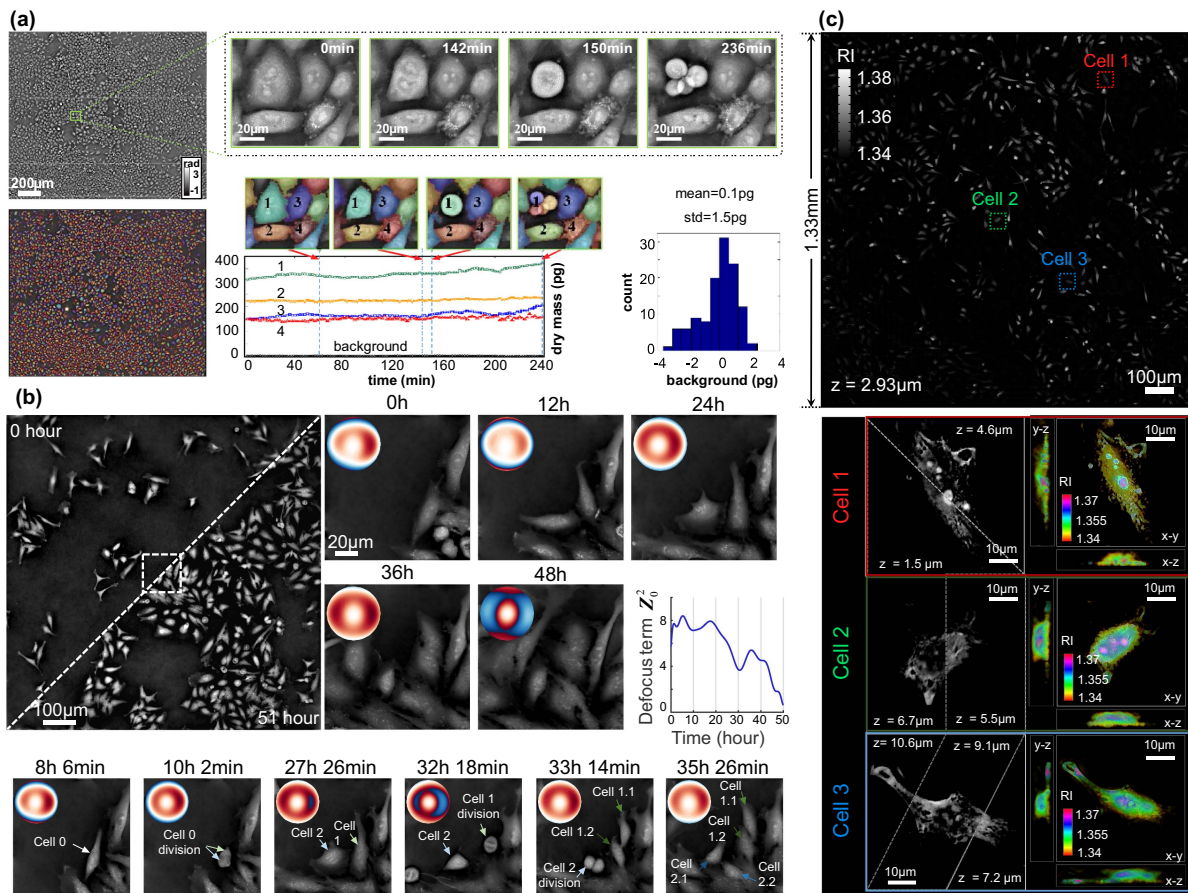


Fig. 6 Label-free cell monitoring and analysis with FPM-QPI. (a) Recovered phase images of unlabeled HeLa cells via the high-speed *in vitro* FPM implementation. The time-lapse phase images can be used to track mitosis of unstained cells and perform automated segmentation and dry mass quantification. (b) Long-term and high-speed live-cell monitoring across 51 h with adaptive optical FPM implementation, in which the spatially and temporally varying aberrations can be effectively corrected. The line plot indicates the focus drift during the process. (c) High-resolution Fourier ptychographic diffraction tomography using both brightfield and darkfield illuminations, in which the 3D refractive index (RI) of a large HeLa cell population is recovered from intensity measurements. 390 nm lateral resolution and 899 nm axial resolution were achieved across an FOV of 1.77 mm^2 . (a) adapted with permission from Ref. [69], © Optical Society of America. (b) adapted from Ref. [55], CC-BY 4.0. (c) adapted from Ref. [76], CC-BY 4.0.

recovered phase is another attractive research. Although a colorful FPM intensity image can be generated by fusing three-channel RGB images, the coherent artifacts in each channel can reduce the color accuracy compared with the regular incoherent images. To address the limitation, one method^[103] used a CycleGAN to translate FPM phase images into virtual bright-field- and fluorescence-stained outputs. A whole-slide virtual IHC staining image with this method is shown in Fig. 7(b). The magnified network outputs are similar to the ground truth

captured by a $20\times/0.75$ NA objective. Currently, a near-infrared FPM implementation^[104] addressed the fading problem in archival slides, where near-infrared illumination was adopted to overcome the absorption variation between stained and faded slides, computationally restoring decade-old H&E stains.

The recovered phase images can also be used for clinical diagnosis. Traditional histological methods relying on chemical staining, although effective, introduce variability due to operator-dependent protocols and potential artifacts from uneven dye

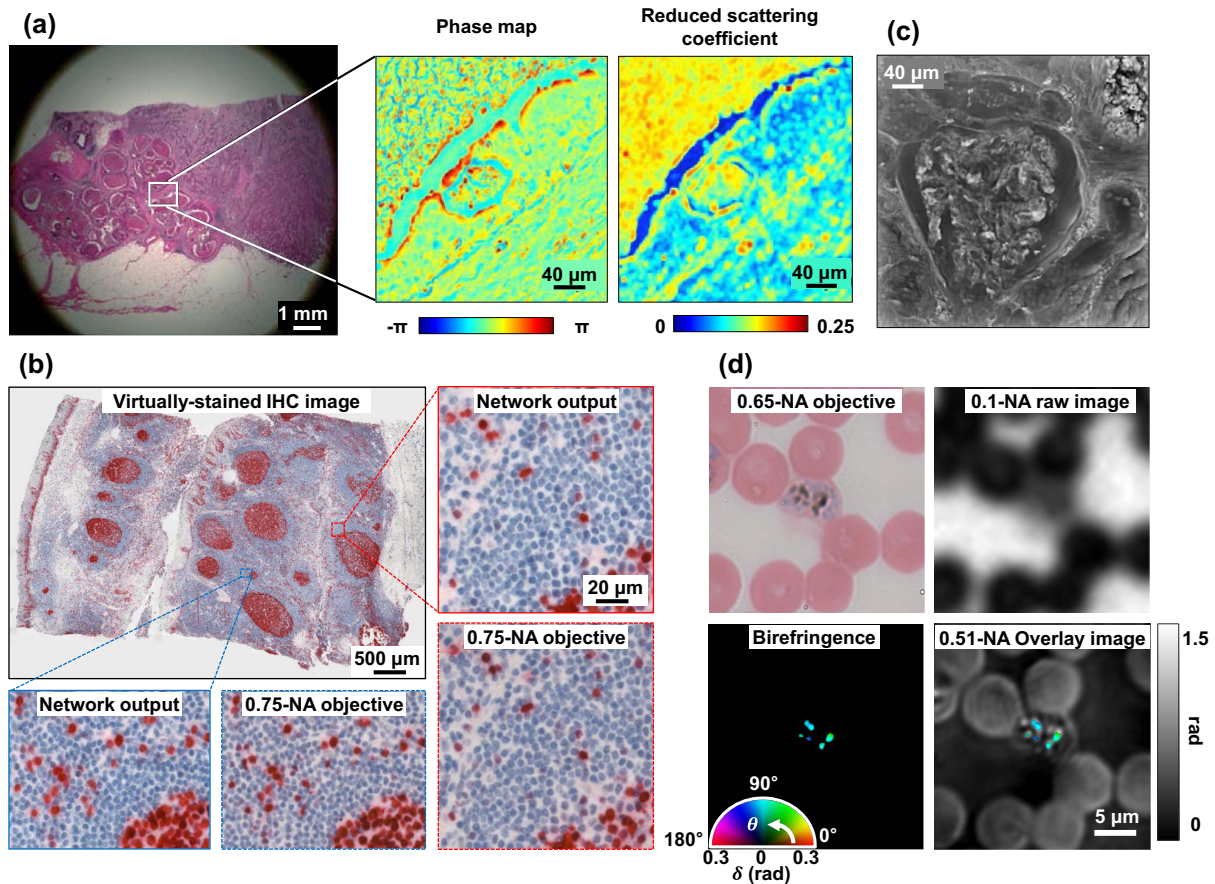


Fig. 7 Digital pathology and clinical diagnosis with FPM-QPI. (a) Large-field complex amplitude images recovered from a stained pathology slide. The recovered phase image shows the phase delays induced by the sample, and the reduced scattering map quantifies how much light has been scattered by the sample, revealing the microscale heterogeneity^[106]. (b) Virtual IHC staining images by utilizing the FPM reconstruction as the input of a network, in which the network outputs show high color fidelity when compared with the measurements of a 0.75 NA objective^[103]. (c) High-resolution phase image of an unstained renal tissue slide, where the morphologies of glomerulus and vasal sections can be observed clearly, showing the potential of FPM-QPI in characterizing the morphology of unstained pathology slides^[107]. (d) Hemozoin detection in a malaria-infected red blood cell (iRBC) using a conventional microscope ($40\times/0.65$ NA) and polarization-sensitive FPM. In the conventional microscope image, hemozoin crystals in the schizont stage iRBC were visualized in dark brown through Wright–Giemsa staining. In PS-FPM, the raw image ($4\times/0.1$ NA) could not resolve hemozoin crystals. After reconstruction, the birefringence signatures (0.51 NA) could be detected, where θ and δ denote the optical-axis retardation and the phase retardation, respectively. By overlaying birefringence information on the recovered phase image, structural information of normal red blood cells and the location of hemozoin crystals could be obtained simultaneously. (a) adapted with permission from Ref. [106], Elsevier: Computerized Medical Imaging and Graphics © 2015. (b) adapted with permission from Ref. [103], © Optical Society of America. (c) adapted from Ref. [107], CC-BY 4.0. (d) adapted from permission from Ref. [112], Copyright 2021, American Chemical Society.

distribution. In contrast, QPI can bypass the need for staining while preserving native structural and biophysical information, including optical thickness and RI variations. The research in Ref. [107] has demonstrated that FPM can provide HR phase images without staining and preserve the morphology of tissue structures. Figure 7(c) shows the phase image of an unstained renal slide, where the morphologies of both glomerulus and vasal sections can be observed with tiny details. Based on the morphology information contained in phase images, the integration of phase-derived fractal biomarkers with machine learning algorithms has shown promise in automating disease classification^[108].

Polarized microscopes have emerged as a powerful tool in clinical diagnosis by enabling quantitative assessment of optically anisotropic biomarkers associated with pathological conditions^[109–111]. The integration of FPM with polarization analysis^[112] significantly enhances diagnostic capabilities through HR birefringence mapping across large FOVs. By reconstructing Jones matrices from phase images, polarization-sensitive FPM quantified birefringence parameters (retardation, optic-axis orientation) at submicron resolution, resolving structural details in pathological crystals. Figure 7(d) shows the hemozoin detection in malaria-infected red blood cells. The overlay image simultaneously provides structure information of the normal red blood cells and the precise location of hemozoin crystals.

4.3. Topography measurement

FPM has established itself as a robust technique for quantitative topography measurement, offering distinct advantages in large-area non-contact profiling with high spatial resolution and nanometer-scale accuracy. Unlike conventional interferometry or scanning probe techniques, FPM achieves wide-field measurements without mechanical scanning, combining sub-nanometer vertical sensitivity with millimeter-scale lateral FOV. This unique combination addresses critical challenges in industrial inspection scenarios.

It is noted that the original FPM implementation is demonstrated with a transmission microscope, which is not applicable for opaque industrial samples such as semiconductor wafers and integrated circuits. To address the limitation, FPM has been demonstrated with reflective system configuration^[113] and has been further developed for higher NAs^[114–118], longer axial measurement arrangements^[120,121], and lower wavelengths^[53,122–125].

Fourier ptychographic topography (FPT)^[117] achieved nanoscale height reconstruction accuracy by synthesizing brightfield and darkfield LED illuminations with reflective configurations. This approach demonstrated a synthetic NA of 0.84 and 750 nm resolution over a 1.2 mm × 1.2 mm FOV on various patterned structures. Figure 8(a) compares the reconstructed surface profile using FPT with conventional optical profilometry results (Zygo NewView 9000, OL: 100×, 0.85 NA), showing excellent agreement in resolving periodic nanostructures with submicron feature sizes. FPM-QPI was also used to detect, count, and topographically measure glass surface defects through the reconstructed quantitative phase images while distinguishing surface defects from particulate contaminants through phase sign inversion^[126]. Figure 8(b) shows the flaw statistics based on 731 flaws identified on the reconstructed phase map of a 44 mm × 19 mm glass surface, where the color scheme represents the number of flaws in squares of size 500 μm × 500 μm and the ellipses denote the average orientation and eccentricity

of these flaws. The defect detection in extreme ultraviolet (EUV) lithography with FPM-QPI was also demonstrated^[123], which successfully identified phase defects in an EUV mask, including 1.5 nm substrate height errors affecting lithographic performance, as shown in Fig. 8(c).

If the sample surface contains step-height structures with significant height variations, it can induce a drastic phase change exceeding 2π , which cannot be unwrapped by algorithms that rely on phase continuity^[119]. To overcome this limitation, a dual-wavelength FPM-QPI approach was developed^[120]. By combining 620 and 633 nm illuminations, the method achieved a synthetic wavelength of 30.19 μm, enabling precise measurement of 1.8 μm steps with ~2 nm standard deviation, as shown in Fig. 8(d). X-ray FPM implementation demonstrated unique advantages for high-energy imaging^[125]. Figure 8(e) demonstrates the nanoscale phase retrieval capability of the proposed objective-lens-scanning X-ray FPM. The reconstructed phase image of an application-specific integrated circuit reveals 47 nm lateral resolution estimated via the 1-bit criterion of Fourier ring correlation (FRC), significantly below the Rayleigh resolution limit (RRL) of 85 nm. It is noted that the recovered phase image of FPM inherently depicts the phase modulation of the measured sample, which is determined by a comprehensively combined effect of the internal structures. Samples like metalenses, whose optical function is achieved by arrangement of a series of nanobricks, can also be characterized by FPM-QPI. Figure 8(f) shows the recovered phase of a 0.59 NA focusing metalens and a focusing vortex metalens^[127], where a large phase deviation existing in the edge area was observed.

5. Outlook

FPM-QPI has emerged as a powerful tool for HR, large-FOV, and label-free imaging, yet several challenges and research trends must be addressed to fully realize its potential.

5.1. Current challenges

5.1.1 Improving the phase transfer function

The optical transfer function (OTF) consists of the modulation transfer function (MTF) and the PTF. The PTF typically reflects the transfer characteristics of an optical system regarding phase variations at different spatial frequencies. Conventional FPM systems often exhibit non-uniform PTFs under non-ideal illumination conditions, leading to incomplete recovery of low-frequency phase information. This limitation reduces phase measurement accuracy, particularly for specimens with linear phase ramps or uniform phase gradients. Meanwhile, the effective bandwidth of the PTF determines the highest spatial resolution in phase imaging. A non-uniform PTF often results in the loss or distortion of high-frequency phase details, such as the edges of subcellular structures. Currently, approaches such as exploiting the defocused phase contrast to circumvent the stringent requirement on the illumination NA imposed by the matched illumination condition have been proposed. This method effectively addressed the reconstruction quality deterioration and RI underestimation problems in conventional FPDT, allowing for more precise HR tomographic imaging^[80]. Another approach attached a flexible, detachable weak-scattering phase modulator to the top of the image sensor, using microparticles on the thin film to spatially encode the complex wavefront of the object. This process converts the phase information into detectable intensity variations, ensuring a uniform frequency

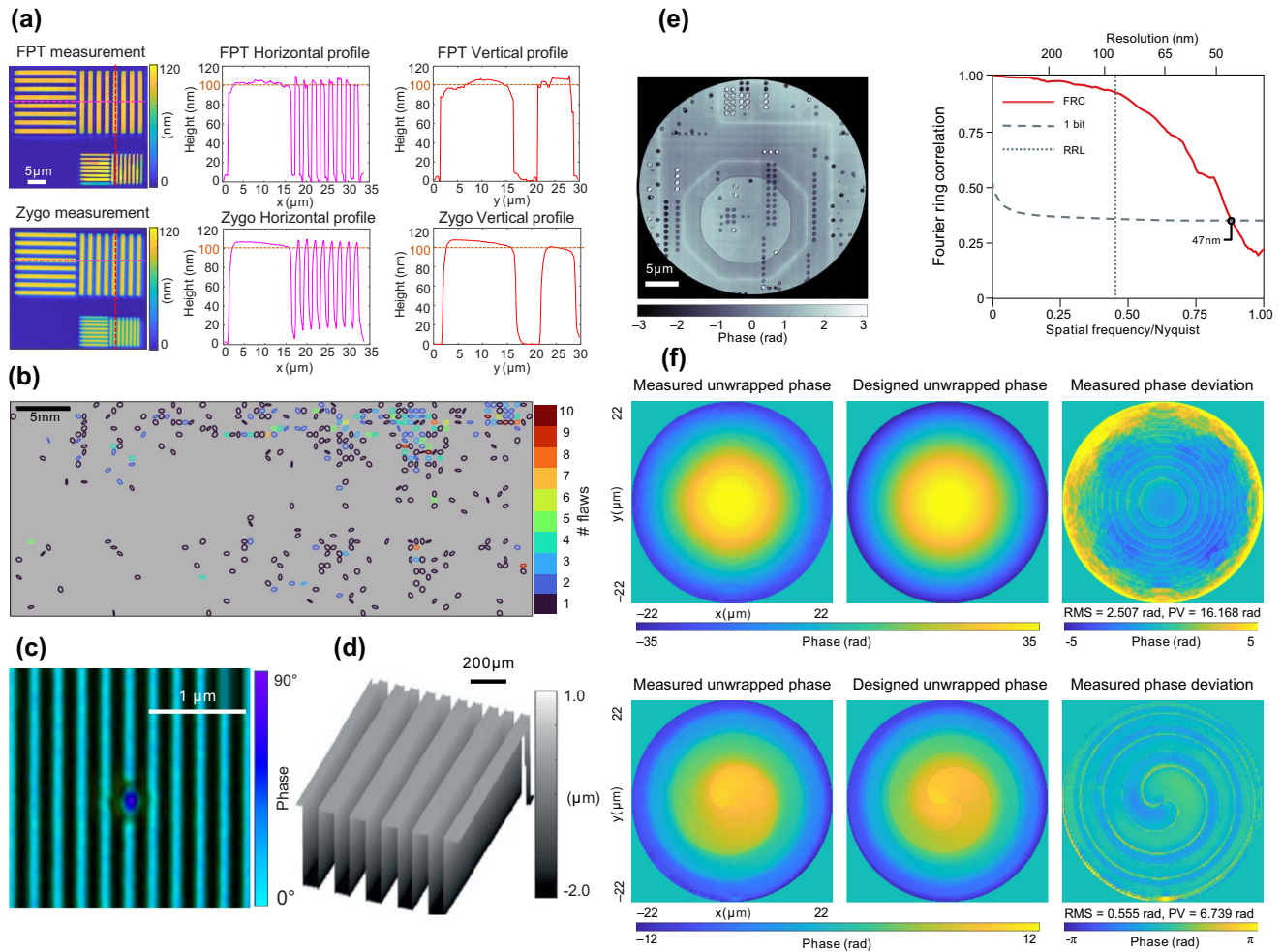


Fig. 8 Topography measurement with FPM-QPI. (a) Topography reconstruction of a high-resolution phase-type sample with reflective Fourier ptychographic topography (FPT). The height profiles are compared with the measurement of an optical profilometer, demonstrating the effectiveness of FPT^[117]. (b) Statistics of 731 flaws identified on the reconstructed phase map of a glass surface. The color scheme represents the number of flaws in squares of size $500\ \mu\text{m} \times 500\ \mu\text{m}$, and the ellipses denote the average orientation and eccentricity of these flaws^[126]. (c) FPM reconstruction of a 1.5 nm defect on an EUV photolithography mask, illustrating the exquisite sensitivity to small phase defects^[123]. (d) 3D topography map of a $1.804\ \mu\text{m}$ step structure using dual-wavelength FPM^[120]. (e) Recovered phase image of an application-specific integrated circuit via X-ray FPM. The resolution is estimated to be 47 nm via the 1-bit criterion of Fourier ring correlation (FRC), that is, the intersection between the red curve and the dashed line. It is better than the Rayleigh resolution limit (RRL), marked by the dotted line^[125]. (f) Comparison of the measured and designed unwrapped phase images of a 0.59 NA focusing metalens and a focusing vortex metalens, where the phase error map reveals the fabrication errors^[127]. (a) adapted with permission from Ref. [117], © Optical Society of America. (b) adapted with permission from Ref. [126], © AIP Publishing. (c) adapted with permission from Ref. [123], © 2018 SPIE. (d) adapted with permission from Ref. [120], © Optical Society of America. (e) adapted from Ref. [125], CC-BY 4.0. (f) adapted with permission from Ref. [127], © Optical Society of America.

response across the entire synthetic bandwidth and correcting RI underestimation issues^[73]. In the future, developing simpler and more efficient methods to achieve an ideal PTF remains a fundamental challenge for advancing high-accuracy QPI.

5.1.2. Calibrating the mismatch of the physical model

The forward imaging model of FPM serves as the foundation for achieving HR reconstruction of targets. However, limitations

imposed by approximations such as the plane wave approximation for spherical wave illumination, the thin object assumption, and the ideal optical system assumption significantly degrade the quality and accuracy of practical image reconstruction. Although existing methods such as EPRY^[50] or full-field pupil recovery^[54] can calibrate the aberrations, they do not work well with weak absorption samples under a relatively high aberration level^[128]. The feature-domain phase retrieval algorithm^[63,129]

provided an alternative avenue to perform blind FPM reconstruction by taking advantage of invariance components of images against mismatches of physical models, but the computational time of hundreds of iterations limits its application in real-time computational microscopy. The development of computation-efficient non-convex phase retrieval algorithms for handling these mismatches is highly desired for high-accuracy QPI.

5.2. Research trends

5.2.1. High-speed and long-term imaging

Although advancements in illumination coding^[69,93] and adaptive optics^[55] have improved the temporal resolution and aberration tolerance of FPM-QPI, the inherent trade-offs between data efficiency and reconstruction fidelity remain unresolved. Strategies to minimize image acquisition often compromise phase accuracy due to sensitivity to illumination misalignment or noise. Additionally, the computational demands of real-time phase retrieval and gigapixel-scale processing limit throughput, especially when scaling to capture datasets required for tracking rare, transient cellular events alongside population-level dynamics. Furthermore, although adaptive aberration correction enhances stability over extended periods, environmental factors such as thermal drift or mechanical vibrations in live-cell cultures still pose risks to long-term imaging consistency, highlighting the need for tighter hardware-software integration. To address these limitations, future efforts could prioritize synergistic innovations in optical systems and computational frameworks. For example, integrating high-speed programmable illumination with deep-learning-based reconstruction algorithms may simultaneously accelerate acquisition, reduce data redundancy, and enhance noise robustness, thereby balancing spatiotemporal resolution without sacrificing the FOV.

5.2.2. Multi-model fusion

Most QPI measurements do not account for the wavelength-dependent RI dispersion of biological samples. Multispectral or hyperspectral FPM could provide valuable insights into phase distributions related to dispersion, enabling more comprehensive sample characterization. In addition, combining FPM with fluorescence or Raman imaging^[130] could enrich functional insights while retaining label-free QPI features.

5.2.3. 3D QPI

2D QPI only provides integrated RI information along one direction, limiting its ability to reveal full structural details. 3D QPI, or IDT, is a promising direction. Developing better forward models and inverse reconstruction algorithms, potentially aided by AI-driven approaches, will be critical for advancing 3D QPI.

5.3. Application trends

5.3.1. Life science

FPM-QPI holds great promise for applications in cell dynamics, cell growth, and tissue optics. For instance, the growing demand for label-free cell monitoring in cell and gene therapy (CGT) highlights the need for non-invasive, real-time imaging techniques to track cell states, proliferation, and differentiation without compromising cell viability. CGT requires multiple cell viability measurements, density, and other parameters during cell culture. Traditional methods use fluorescent labeling to

obtain these parameters, but the stained cells are already contaminated and cannot be reused, leading to wastage of cells. We anticipate that the high-SBP QPI capability of FPM can completely establish it to replace the fluorescent labeling methods to obtain the desired cell parameters.

5.3.2. Clinical medicine

To achieve clinical deployment, FPM-based QPI must meet additional requirements such as high throughput and cost-effectiveness. Emerging applications in drug screening^[131] and tissue diagnosis^[108,112] show potential, but challenges remain in understanding tissue optical properties. Current limitations include the lack of experimental methods to measure cell and tissue optical properties and the variability of refractive indices across different organs and within tissues. Ideal measurements should provide scattering properties from the organelle to organ scales, a goal that has yet to be fully realized.

5.3.3. Surface metrology

Current FPM-based QPI systems for topographic metrology remain constrained by fundamental trade-offs between spatial/axial resolution, temporal stability, and operational practicality. While synthetic aperture strategies enhance lateral resolution, their reliance on sequential illumination scanning inherently limits temporal resolution and introduces vibration sensitivity in industrial environments. The extended DOF capabilities achieved through computational refocusing conversely amplify phase retrieval ambiguities near steep edges. Future progress may exploit hybrid interferometric-FPM architectures with spectrally engineered illumination to decouple sensitivity from mechanical scanning, potentially enabling simultaneous $<\lambda/100$ axial resolution and kHz-scale acquisition rates.

Disclosures

The authors declare no conflicts of interest.

Acknowledgments

This work was supported by the National Natural Science Foundation of China (No. 62275020).

References

1. J. Mertz, *Introduction to Optical Microscopy* (Cambridge University Press, 2019).
2. Y. Park, C. Depeursinge, and G. Popescu, "Quantitative phase imaging in biomedicine," *Nat. Photonics* **12**, 578 (2018).
3. T. Nguyen, *et al.*, "Quantitative phase imaging: recent advances and expanding potential in biomedicine," *ACS Nano* **16**, 11516 (2022).
4. G. Zheng, R. Horstmeyer, and C. Yang, "Wide-field, high-resolution Fourier ptychographic microscopy," *Nat. Photonics* **7**, 739 (2013).
5. X. Ou, *et al.*, "Quantitative phase imaging via Fourier ptychographic microscopy," *Opt. Lett.* **38**, 4845 (2013).
6. E. Abbe, "Beiträge zur Theorie des Mikroskops und der mikroskopischen Wahrnehmung," *Arch. Mikrosk. Anat.* **9**, 413 (1873).
7. J. Goodman, *Introduction to Fourier Optics* (Roberts and Company Publishers, 2005).
8. M. Abramowitz, *Contrast Methods in Microscopy: Transmitted Light* (Olympus Corporation Publishing, 1987).
9. F. Zernike, "Phase contrast, a new method for the microscopic observation of transparent objects," *Physica* **9**, 686 (1942).

10. F. Zernike, "How I discovered phase contrast," *Science* **121**, 345 (1955).
11. R. Allen, G. Davida, and G. Nomarski, "The Zeiss-Nomarski differential interference equipment for transmitted-light microscopy," *Z. Wiss. Mikrosk* **69**, 193 (1969).
12. N. Jaccard, *et al.*, "Automated method for the rapid and precise estimation of adherent cell culture characteristics from phase contrast microscopy images," *Biotechnol. Bioeng.* **111**, 504 (2014).
13. Z. Yin, T. Kanade, and M. Chen, "Understanding the phase contrast optics to restore artifact-free microscopy images for segmentation," *Med. Image Anal.* **16**, 1047 (2012).
14. T. Zangle and M. Teitell, "Live-cell mass profiling: an emerging approach in quantitative biophysics," *Nat. Methods* **11**, 1221 (2014).
15. R. Barer, "Determination of dry mass, thickness, solid and water concentration in living cells," *Nature* **172**, 1097 (1953).
16. G. Popescu, *et al.*, "Optical imaging of cell mass and growth dynamics," *Am. J. Physiol.* **295**, C538 (2008).
17. M. Mir, *et al.*, "Optical measurement of cycle-dependent cell growth," *Proc. Natl. Acad. Sci. USA* **108**, 13124 (2011).
18. K. Kim, *et al.*, "Three-dimensional label-free imaging and quantification of lipid droplets in live hepatocytes," *Sci. Rep.* **6**, 36815 (2016).
19. Y. Li, *et al.*, "Quantitative investigation on morphology and intracellular transport dynamics of migrating cells," *Appl. Opt.* **58**, G162 (2019).
20. R. Barer, "Interference microscopy and mass determination," *Nature* **169**, 366 (1952).
21. C. Schwarz, Y. Kuznetsova, and S. Brueck, "Imaging interferometric microscopy," *Opt. Lett.* **28**, 1424 (2003).
22. Y. Kuznetsova, A. Neumann, and S. Brueck, "Imaging interferometric microscopy—approaching the linear systems limits of optical resolution," *Opt. Exp.* **15**, 6651 (2007).
23. G. Popescu, *et al.*, "Diffraction phase microscopy for quantifying cell structure and dynamics," *Opt. Lett.* **31**, 775 (2006).
24. B. Bhaduri, *et al.*, "Diffraction phase microscopy: principles and applications in materials and life sciences," *Adv. Opt. Photonics* **6**, 57 (2014).
25. E. Cuche, F. Bevilacqua, and C. Depeursinge, "Digital holography for quantitative phase-contrast imaging," *Opt. Lett.* **24**, 291 (1999).
26. E. Cuche, P. Marquet, and C. Depeursinge, "Spatial filtering for zero-order and twin-image elimination in digital off-axis holography," *Appl. Opt.* **39**, 4070 (2000).
27. B. Kemper and G. Bally, "Digital holographic microscopy for live cell applications and technical inspection," *Appl. Opt.* **47**, A52 (2008).
28. Z. Huang and L. Cao, "Quantitative phase imaging based on holography: trends and new perspectives," *Light Sci. Appl.* **13**, 145 (2024).
29. M. Born, *et al.*, *Principles of Optics: Electromagnetic Theory of Propagation, Interference and Diffraction of Light* (Cambridge University Press, 1999).
30. Z. Wang, *et al.*, "Spatial light interference microscopy (SLIM)," *Opt. Exp.* **19**, 1016 (2011).
31. P. Bon, *et al.*, "Quadriwave lateral shearing interferometry for quantitative phase microscopy of living cells," *Opt. Exp.* **17**, 13080 (2009).
32. B. Bhaduri, *et al.*, "Diffraction phase microscopy with white light," *Opt. Lett.* **37**, 1094 (2012).
33. M. R. Teague, "Irradiance moments: their propagation and use for unique retrieval of phase," *J. Opt. Soc. Am.* **72**, 1199 (1982).
34. M. R. Teague, "Deterministic phase retrieval: a Green's function solution," *J. Opt. Soc. Am. A.* **73**, 1434 (1983).
35. C. Zuo, *et al.*, "Transport of intensity equation: a tutorial," *Opt. Lasers Eng.* **135**, 106187 (2020).
36. L. Tian and L. Waller, "Quantitative differential phase contrast imaging in an LED array microscope," *Opt. Exp.* **23**, 11394 (2015).
37. Y. Fan, *et al.*, "Optimal illumination scheme for isotropic quantitative differential phase contrast microscopy," *Photonics Res.* **7**, 890 (2019).
38. S. Liu, *et al.*, "Single-shot quantitative differential phase contrast imaging combined with programmable polarization multiplexing illumination," *Opt. Lett.* **48**, 3559 (2023).
39. R. Gerchberg and W. Saxton, "Phase determination for image and diffraction plane pictures in the electron microscope," *Optik* **34**, 275 (1971).
40. J. R. Fienup, "Phase retrieval algorithms: a comparison," *Appl. Opt.* **21**, 2758 (1982).
41. A. Lohmann, *et al.*, "Space-bandwidth product of optical signals and systems," *J. Opt. Soc. Am. A.* **13**, 470 (1996).
42. M. Ryle and A. Hewish, "The synthesis of large radio telescopes," *Mon. Not. R. Astron. Soc.* **120**, 220 (1960).
43. L. Bian, *et al.*, "Content adaptive illumination for Fourier ptychography," *Opt. Lett.* **39**, 6648 (2014).
44. K. Guo, *et al.*, "Optimization of sampling pattern and the design of Fourier ptychographic illuminator," *Opt. Exp.* **23**, 6171 (2015).
45. J. Sun, *et al.*, "Sampling criteria for Fourier ptychographic microscopy in object space and frequency space," *Opt. Exp.* **24**, 15765 (2016).
46. J. Rodenburg and H. Faulkner, "A phase retrieval algorithm for shifting illumination," *Appl. Phys. Lett.* **85**, 4795 (2004).
47. H. Faulkner and J. Rodenburg, "Movable aperture lensless transmission microscopy: a novel phase retrieval algorithm," *Phys. Rev. Lett.* **93**, 203903 (2004).
48. L. Yeh, *et al.*, "Experimental robustness of Fourier ptychography phase retrieval algorithms," *Opt. Exp.* **23**, 33214 (2015).
49. Z. Bian, S. Dong, and G. Zheng, "Adaptive system correction for robust Fourier ptychographic imaging," *Opt. Exp.* **21**, 32400 (2013).
50. X. Ou, G. Zheng, and C. Yang, "Embedded pupil function recovery for Fourier ptychographic microscopy," *Opt. Exp.* **22**, 1960 (2014).
51. L. Tian, *et al.*, "Multiplexed coded illumination for Fourier ptychography with an LED array microscope," *Biomed. Opt. Exp.* **5**, 2376 (2014).
52. C. Zuo, J. Sun, and Q. Chen, "Adaptive step-size strategy for noise-robust Fourier ptychographic microscopy," *Opt. Exp.* **24**, 20724 (2016).
53. V. Pham, *et al.*, "Momentum Fourier ptychographic topography," *Opt. Laser Eng.* **180**, 108276 (2024).
54. P. Song, *et al.*, "Full-field Fourier ptychography (FFP): spatially varying pupil modeling and its application for rapid field-dependent aberration metrology," *APL Photon.* **4**, 050802 (2019).
55. Y. Shu, *et al.*, "Adaptive optical quantitative phase imaging based on annular illumination Fourier ptychographic microscopy," *PhotoniX* **3**, 24 (2022).
56. A. Zhou, *et al.*, "Fast and robust misalignment correction of Fourier ptychographic microscopy for full field of view reconstruction," *Biomed. Opt. Exp.* **26**, 23661 (2018).
57. S. Zhang, *et al.*, "A simply equipped Fourier ptychography platform based on an industrial camera and telecentric objective," *Sensors* **19**, 4913 (2019).
58. L. Yeh *et al.*, "Experimental robustness of Fourier ptychography phase retrieval algorithm," *Opt. Exp.* **23**, 33214 (2015).
59. J. Sun, *et al.*, "Efficient positional misalignment correction method for Fourier ptychographic microscopy," *Biomed. Opt. Exp.* **7**, 1336 (2016).
60. R. Eckert, Z. Phillips, and L. Waller, "Efficient illumination angle self-calibration in Fourier ptychography," *Appl. Opt.* **57**, 5434 (2018).

61. C. Zheng, *et al.*, "Robust Fourier ptychographic microscopy via a physics-based defocusing strategy for calibrating angle-varied LED illumination," *Biomed. Opt. Exp.* **13**, 1581 (2022).
62. C. Zheng, *et al.*, "Robust full-pose-parameter estimation for the LED array in Fourier ptychographic microscopy," *Biomed. Opt. Exp.* **13**, 4468 (2022).
63. S. Zhang, T. Berendschot, and J. Zhou, "ELFPIE: an error-laxity Fourier ptychographic iterative engine," *Signal Process* **210**, 109088 (2023).
64. L. Bian, *et al.*, "Fourier ptychographic reconstruction using Wirtinger flow optimization," *Opt. Exp.* **23**, 4856 (2015).
65. L. Bian, *et al.*, "Fourier ptychographic reconstruction using Poisson maximum likelihood and truncated Wirtinger gradient," *Sci. Rep.* **6**, 27384 (2016).
66. Y. Zhang, P. Song, and Q. Dai, "Fourier ptychographic microscopy using a generalized Anscombe transform approximation of the mixed Poisson-Gaussian likelihood," *Opt. Exp.* **25**, 168 (2017).
67. Y. Zhang, *et al.*, "Fourier ptychographic microscopy with sparse representation," *Sci. Rep.* **7**, 8664 (2017).
68. Y. Zhang, *et al.*, "Group-based sparse representation for Fourier ptychography microscopy," *Opt. Commun.* **404**, 55 (2017).
69. L. Tian, *et al.*, "Computational illumination for high-speed *in vitro* Fourier ptychographic microscopy," *Optica* **2**, 904 (2015).
70. G. Jagatap, *et al.*, "Sample efficient Fourier ptychography for structured data," *IEEE Trans. Comput. Imaging* **6**, 344 (2019).
71. C. Zheng, *et al.*, "Single-shot Fourier ptychographic microscopy with isotropic lateral resolution via polarization-multiplexed LED illumination," *Biomed. Opt. Exp.* **15**, 672 (2024).
72. J. Sun, *et al.*, "Single-shot quantitative phase microscopy based on color-multiplexed Fourier ptychography," *Opt. Lett.* **43**, 3365 (2018).
73. R. Wang, *et al.*, "Spatially-coded Fourier ptychography: flexible and detachable coded thin films for quantitative phase imaging with uniform phase transfer characteristics," *Adv. Opt. Mater.* **12**, 2323028 (2024).
74. E. Wolf, "Three-dimensional structure determination of semi-transparent objects from holographic data," *Opt. Commun.* **1**, 153 (1969).
75. R. Horstmeyer, *et al.*, "Diffraction tomography with Fourier ptychography," *Optica* **3**, 827 (2019).
76. C. Zuo, *et al.*, "Wide-field high-resolution 3D microscopy with Fourier ptychographic diffraction tomography," *Opt. Lasers. Eng.* **128**, 106003 (2020).
77. S. Zhou, *et al.*, "Accelerated Fourier ptychographic diffraction tomography with sparse annular LED illuminations," *J. Biophot.* **15**, e202100272 (2021).
78. M. Lee, *et al.*, "Isotropically resolved label-free tomographic imaging based on tomographic moulds for optical trapping," *Light Sci. Appl.* **10**, 1 (2021).
79. N. Zhou, *et al.*, "Quasi-isotropic high-resolution Fourier ptychographic diffraction tomography with opposite illuminations," *ACS Photonics* **10**, 2461 (2023).
80. S. Zhou, *et al.*, "Transport-of-intensity Fourier ptychographic diffraction tomography: defying the matched illumination condition," *Optica* **9**, 1362 (2022).
81. L. Tian and L. Waller, "3D intensity and phase imaging from light field measurements in an LED array microscope," *Optica* **2**, 104 (2015).
82. S. Chowdhury, *et al.*, "High-resolution 3D refractive index microscopy of multiple-scattering samples from intensity images," *Optica* **6**, 1211 (2019).
83. M. Chen, *et al.*, "Multi-layer Born multiple-scattering model for 3D phase microscopy," *Optica* **7**, 394 (2020).
84. S. Song, *et al.*, "Polarization-sensitive intensity diffraction tomography," *Light Sci. Appl.* **12**, 124 (2023).
85. A. Kappeler, *et al.*, "Ptychnet: CNN based Fourier ptychography," in *2017 IEEE International Conference on Image Processing ICIP* (2017), p. 1712.
86. T. Nguyen, *et al.*, "Deep learning approach to Fourier ptychographic microscopy," *Opt. Exp.* **26**, 26470 (2018).
87. J. Zhang, *et al.*, "Fourier ptychographic microscopy reconstruction with multiscale deep residual network," *Opt. Exp.* **27**, 8612 (2019).
88. Y. Xue, *et al.*, "Reliable deep-learning-based phase imaging with uncertainty quantification," *Optica* **6**, 618 (2019).
89. D. Ulyanov, A. Vedaldi, and V. Lempitsky, "Deep image prior," in *Proceedings of the IEEE Conference on Computer Vision and Pattern Recognition* (2018), p. 9446.
90. F. Shamshad, A. Hanif, and A. Ahmed, "Subsampled Fourier ptychography using pretrained invertible and untrained network priors," arXiv preprint, arXiv:2005.07026 (2020).
91. Q. Chen, D. Huang, and R. Chen, "Fourier ptychographic microscopy with untrained deep neural network priors," *Opt. Exp.* **30**, 39597 (2022).
92. F. Wang, *et al.*, "Phase imaging with an untrained neural network," *Light Sci Appl* **9**, 77 (2020).
93. Z. Zhang, *et al.*, "Sparse phase retrieval using a physics-informed neural network for Fourier ptychographic microscopy," *Opt. Lett.* **47**, 4909 (2022).
94. R. Sun, *et al.*, "Hybrid deep-learning and physics-based neural network for programmable illumination computational microscopy," *Adv. Photonics Nexus* **3**, 056003 (2024).
95. N. Chen, *et al.*, "Differentiable imaging: a new tool for computational optical imaging," *Adv. Phys. Res.* **2**, 2200118 (2023).
96. N. Chen, D. Brady, and E. Lam, *Differentiable Imaging: Progress, Challenges, and Outlook* (2025).
97. S. Jiang, *et al.*, "Solving Fourier ptychographic imaging problems via neural network modeling and TensorFlow," *Biomed. Opt. Exp.* **9**, 3306 (2018).
98. D. Yang, *et al.*, "Fourier ptychography multi-parameter neural network with composite physical priori optimization," *Biomed. Opt. Exp.* **13**, 2739 (2022).
99. R. Sun, *et al.*, "Unsupervised adaptive coded illumination Fourier ptychographic microscopy based on a physical neural network," *Biomed. Opt. Exp.* **14**, 4205 (2023).
100. C. Ni, *et al.*, "Uncertainty-aware Fourier ptychography," *Optica Open. Preprint* (2025).
101. R. Sun, *et al.*, "Batch-FPM: random batch-update multi-parameter physical Fourier ptychography neural network," arXiv preprint, arXiv:2408.13782 (2024).
102. A. Muthumbi, *et al.*, "Learned sensing: jointly optimized microscope hardware for accurate image classification," *Biomed. Opt. Exp.* **10**, 6351 (2019).
103. R. Wang, *et al.*, "Virtual brightfield and fluorescence staining for Fourier ptychography via unsupervised deep learning," *Opt. Lett.* **45**, 5405 (2020).
104. H. Chae, *et al.*, "Restoring H&E stain in faded slides via phase-to-color virtual staining in near-infrared," *APL Photon.* **9**, 106112 (2024).
105. Y. Su, *et al.*, "Advancing tumor budding detection with Fourier ptychography microscopy," arXiv preprint, arXiv: 2503.16170, (2025).
106. R. Horstmeyer, *et al.*, "Digital pathology with Fourier ptychography," *Comput. Med. Imag. Grap.* **42**, 38 (2015).
107. M. Valentino, *et al.*, "Beyond conventional microscopy: observing kidney tissues by means of Fourier ptychography," *Front. Physiol.* **14**, 1120099 (2023).
108. V. Bianco, *et al.*, "Classifying breast cancer and fibroadenoma tissue biopsies from paraffined stain-free slides by fractal biomarkers in Fourier ptychographic microscopy," *Comput. Struct. Biotechnol. J.* **24**, 225 (2024).
109. M. Rajadhyakasha, *et al.*, "Confocal examination of nonmelanoma cancers in thick skin excisions to potentially guide

- Mohs micrographic surgery without frozen histopathology,” *J. Invest. Dermatol.* **117**, 1137 (2001).
110. H. Su, M. Lee, and W. Lee, “Surface modification of alignment layer by ultraviolet irradiation to dramatically improve the detection limit of liquid-crystal-based immunoassay for the cancer biomarker CA125,” *J. Biomed. Opt.* **20**, 057004 (2015).
 111. C. Pirmstill and G. Cote, “Malaria diagnosis using a mobile phone polarized microscope,” *Sci. Rep.* **5**, 13368 (2015).
 112. S. Song, *et al.*, “Large-area, high-resolution birefringence imaging with polarization-sensitive Fourier ptychographic microscopy,” *ACS Photonics*, **8**, 158 (2021).
 113. S. Pacheco, *et al.*, “Transfer function analysis in epi-illumination Fourier ptychography,” *Opt. Lett.* **40**, 5343 (2015).
 114. S. Pacheco, G. Zheng, and R. Liang, “Reflective Fourier ptychography,” *J. Biomed. Opt.* **21**, 026010 (2016).
 115. K. Guo, S. Dong, and G. Zheng, “Fourier ptychography for brightfield, phase, darkfield, reflective, multi-slice, and fluorescence imaging,” *IEEE J. Sel. Top. Quantum Electron.* **22**, 77 (2016).
 116. H. Lee, B. Chon, and H. Ahn, “Reflective Fourier ptychographic microscopy using a parabolic mirror,” *Opt. Exp.* **27**, 34382 (2019).
 117. H. Wang, *et al.*, “Fourier ptychographic topography,” *Opt. Express* **31**, 11007 (2023).
 118. H. Ahn and B. Chon, “Reflective Fourier ptychographic microscopy using segmented mirrors and a mask,” *Curr. Opt. Photonics* **5**, 40 (2021).
 119. H. Abdul-Rahamn, *et al.*, “Fast and robust three-dimensional best path phase unwrapping algorithm,” *Appl. Opt.* **46**, 6623 (2007).
 120. G. Choi *et al.*, “Dual-wavelength Fourier ptychography using a single LED,” *Opt. Lett.* **43**, 3526 (2018).
 121. Q. Hao, *et al.*, “Dual-wavelength Fourier ptychographic microscopy for topographic measurement,” *Opt. Express*, **32**, 6684 (2024).
 122. K. Park, *et al.*, “High numerical aperture reflective deep ultraviolet Fourier ptychographic microscopy for nanofeature imaging,” *APL Photonics* **7**, 096105 (2022).
 123. A. Wojdyla, *et al.*, “EUV photolithography mask inspection using Fourier ptychography,” *Image Sens. Technol. Mater. Dev. Syst. Appl. V*, **10656**, 106560W (2018).
 124. C. Gu, *et al.*, “Enhanced EUV mask imaging using Fourier ptychographic microscopy,” in *SPIE Advanced Lithography* (2025), p. 31424.
 125. K. Wakonig *et al.*, “X-ray Fourier ptychography,” *Sci. Adv.* **5**, eaav0282 (2019).
 126. K. Tekseth, *et al.*, “Mapping surface flaws on float glass through Fourier ptychographic quantitative phase imaging,” *Appl. Phys. Lett.* **123**, 021108 (2023).
 127. C. Zheng, *et al.*, “High-space-bandwidth product characterization of metalenses by information fusion of multi-angle illumination,” *Optica* **12**, 374 (2025).
 128. R. Cao, C. Shen, and C. Yang, “High-resolution, large field-of-view label-free imaging via aberration-corrected, closed-form complex field reconstruction,” *Nat. Commun.* **15**, 4713 (2024).
 129. S. Zhang, *et al.*, “High-fidelity computational microscopy via feature-domain phase retrieval,” *Adv. Sci.* **12**, 2413975 (2025).
 130. S. Heuke, *et al.*, “Coherent anti-stokes Raman Fourier ptychography,” *Opt. Exp.* **27**, 23497 (2019).
 131. A. Chan, *et al.*, “Parallel Fourier ptychographic microscopy for high-throughput screening with 96 cameras (96 eyes),” *Sci. Rep.* **9**, 11114 (2019).